

# **Aerosol-meteorology feedback diminishes the trans-boundary transport of black carbon into the Tibetan Plateau**

Yuling Hu<sup>a</sup>, Shichang Kang<sup>b, c, \*</sup>, Haipeng Yu<sup>a</sup>, Junhua Yang<sup>b</sup>, Mukesh Rai<sup>b</sup>, Xiufeng  
Yin<sup>b</sup>, Xintong Chen<sup>b</sup>, Pengfei Chen<sup>b</sup>

<sup>a</sup>Key Laboratory of Land Surface Process and Climate Change in Cold and Arid  
Regions, Northwest Institute of Eco-Environment and Resources, Chinese Academy of  
Sciences, Lanzhou 730000, China

<sup>b</sup>State Key Laboratory of Cryospheric Science, Northwest Institute of Eco-Environment  
and Resources, Chinese Academy of Sciences, Lanzhou 730000, China

<sup>c</sup>University of Chinese Academy of Sciences, Beijing 100049, China

Correspondence to: Shichang Kang ([shichang.kang@lzb.ac.cn](mailto:shichang.kang@lzb.ac.cn))

## **Abstract**

Black carbon (BC) exerts potential effect on climate, especially in the Tibetan Plateau (TP), where the cryosphere and environment are very sensitive to climate change. The TP saw a record-breaking aerosol pollution event during the period from April 20 to May 10, 2016. This paper investigated the meteorological causes of the severe aerosol pollution event, the trans-boundary transport flux of BC, and the aerosol-meteorology feedback and its effect on the trans-boundary transport flux of BC during this severe aerosol pollution event via using observational and reanalysis datasets and simulation from the coupled meteorology and aerosol/chemistry model (WRF-Chem). By analyzing weather maps derived from the reanalysis dataset, it is found that the plateau

vortex and southerly winds were key factors that contributed to the severe aerosol pollution event. Subsequently, with the good performance of WRF-Chem model on the spatiotemporal characteristics of meteorological conditions and aerosols, the transboundary transport flux of BC during the pollution event was investigated. The results show that the vertically integrated cross-Himalayan transport flux of BC decreases from west to east, with the largest transport flux of  $20.8 \text{ mg m}^{-2} \text{ s}^{-1}$  occurring at the deepest mountain valley in southwestern TP. Results from simulations with and without aerosol-meteorology feedback show that aerosols induce significant changes in meteorological conditions in the southern TP and the Indo-Gangetic Plain (IGP), with the atmospheric stratification being more stable and the planetary boundary layer height decreasing in both regions, and 10-m wind speed increasing in the southern TP but decreasing in the IGP. Changes in meteorological conditions in turn lead to a decrease in surface BC concentration with a value up to  $0.16 \text{ }\mu\text{g/m}^3$  (50%) in the southern TP and an increase of surface BC concentration with a value up to  $2.2 \text{ }\mu\text{g/m}^3$  (75%) in the IGP. By excavating the impact of aerosol-meteorology feedback on the transboundary transport flux of BC, it has been acquired that the aerosol-meteorology feedback decreases the vertically integrated transboundary transport flux of BC from the central and western Himalayas towards the TP. This study not only provides crucial policy implications for mitigating glacier melt caused by aerosols over the TP but also is of great significance to the ecological environment protection for the TP.

**Keywords:** Tibetan Plateau; Black carbon; Transport flux; Aerosol-meteorology feedback; WRF-Chem

## 1 Introduction

Known as “the Third Pole”, the Tibetan Plateau (TP) plays a significant role in driving climate change in the Northern Hemisphere and even the globe through thermal and dynamical forcing (Wu et al., 2007; Lau et al., 2006). What’s more, with the concentrated glacier and snow cover outside of the polar regions, the TP supplies a substantial portion of the water demand for almost 2 billion people (Yao et al., 2022). However, numerous studies from recent years have reported that the TP experienced significant and rapid climate warming during the last few decades (Kang et al., 2010; You et al., 2016; You et al., 2021). As a result of this intensive warming, glaciers over the TP have undergone unprecedented widespread losses and accelerated retreats (Kang et al., 2010; Yao et al., 2007). Besides high levels of greenhouse gases (Duan et al., 2006), other factors like atmospheric heating and snow albedo reduction due to absorbing aerosols also contribute a large portion to this climate warming and glacier retreat (Xu et al., 2009; Zhang et al., 2021; Kang et al., 2019b). However, with an average elevation exceeding 4 km, the TP is relatively undisturbed by human activities and is one of the most pristine regions on the earth. Hence, aerosols over the TP are mainly sourced from its surrounding regions (Kang et al., 2019b). Particularly, with nearly half of the world’s population and heavy industry, South and East Asia adjacent to the TP are the world’s hotspots for aerosol pollution (Lelieveld et al., 2016). Driven by atmospheric circulation, aerosols over South and East Asia can transport to the TP, and then exert a striking effect on the hydrological cycle and climate (Wu et al., 2008; Ramanathan et al., 2005; Liu et al., 2014). Previous studies indicated that aerosols

over the TP are primarily transported via typical long-distance trans-boundary transport events (Kang et al., 2019a). It is therefore paramount to excavate the meteorological causes of the severe aerosol pollution event as well as the trans-boundary transport flux of aerosols during the severe aerosol pollution event.

Black carbon (BC) exerts a substantial impact on climate through several mechanisms, including heating the atmosphere by absorbing shortwave and longwave radiation, darkening the surface of snow and ice and accelerating the melt of the cryosphere, and modifying the optical and microphysical properties of clouds (Kang et al., 2019b; Ramanathan and Carmichael, 2008; Flanner et al., 2007; Skiles et al., 2018). Estimation from the literature shows that BC is the second most important type of human forcing after carbon dioxide, with a global climate forcing of  $1.2 \text{ W m}^{-2}$  (Ramanathan and Carmichael, 2008; Chung et al., 2005). Moreover, the radiative forcing of BC in snow and ice is approximately twice as high as that of carbon dioxide and other types of anthropogenic forcing (Flanner et al., 2007; Qian et al., 2011; Hansen and Nazarenko, 2004). Particularly, as a sensitive area to global climate change, the TP has experienced an increase in BC content in recent years (Xu et al., 2009). It is evident that BC plays a substantial role in the climate and environmental change over the TP. However, previous studies primarily focused on the origin of BC and its climatic effect over the TP on annual and seasonal timescales (Yang et al., 2018; Hu et al., 2022; Rai et al., 2022). With respect to the trans-boundary transport flux of BC towards the TP during the severe aerosol pollution event on the synoptic scale, there is still a blank, which should be studied urgently.

Severe aerosol pollution events are usually accompanied by complex aerosol-meteorology feedback. Moreover, numerous studies have revealed that the aerosol-meteorology feedback has a substantial effect on surface aerosol concentration (Wu et al., 2019; Zhang et al., 2018; Zhao et al., 2017; Hong et al., 2020; Chen et al., 2019a; Gao et al., 2016). For instance, some studies analyzed the aerosol-meteorology feedback and its effect on surface PM<sub>2.5</sub> concentration during heavy aerosol pollution events in winter in northern China, and found that positive aerosol-meteorology feedback can increase the surface PM<sub>2.5</sub> concentration (Li et al., 2020; Qiu et al., 2017; Wu et al., 2019). Nonetheless, other studies suggested that the aerosol-meteorology feedback can reduce the surface PM<sub>2.5</sub> concentration in Beijing (Zheng et al., 2015; Gao et al., 2016). Based on in-situ observational data, Zhong et al. (2018) analyzed the aerosol-meteorology feedback during several air pollution events in Beijing and concluded that 70% of the increase in surface PM<sub>2.5</sub> concentration in the cumulative outbreak stage of haze could be attributed to the aerosol-meteorology feedback. The above-mentioned studies mainly focused on the economically developed central and eastern China regions. However, the TP has a very high altitude and complex topography along with a tough environment and scarce in-situ observational data. Systematic and comprehensive studies on aerosol-meteorology feedback in this region are still lacking and need urgent investigation. Furthermore, what effect the aerosol-meteorology feedback has on the trans-boundary transport flux of BC also remains unclear, which also worth an in-depth study. Therefore, in this study, we attempt to investigate the meteorological causes of the severe aerosol pollution event, the trans-boundary transport flux of BC, the aerosol-

meteorology feedback and its effect on the trans-boundary transport flux of BC during the severe aerosol pollution event using observational and reanalysis datasets, and numerical simulation with the advanced regional climate-chemistry model, the Weather Research and Forecasting with Chemistry (WRF-Chem). This study not only provides crucial policy implications for mitigating glacier melt caused by aerosols over the TP, but also is of great significance to the ecological environment protection for the TP. The paper is organized as follows: in the first section, an introduction is presented to state the importance of this study and to summarize the previous studies related to aerosol-meteorology feedback. Section 2 introduces the data, the definition of an aerosol pollution event, and the WRF-Chem model configuration along with experimental details. In section 3, the meteorological causes of the severe aerosol pollution event, the trans-boundary transport flux of BC, the aerosol-meteorology feedback and its effect on the trans-boundary transport flux of BC during the severe aerosol pollution event are investigated. Section 4 presented the main conclusions.

## **2. Data, Definition of an aerosol pollution event, WRF-Chem model configuration, Emissions, and Experimental details**

### *2.1 Data*

#### *2.1.1 ERA-Interim*

To explore the meteorological causes of the severe aerosol pollution event, the geopotential height, air temperature (T), and wind fields at 500 hPa with a horizontal resolution of  $0.05^{\circ} \times 0.05^{\circ}$  during the period from April 20 to May 10, 2016 are from the

European Center for Medium-Range Weather Forecasts interim reanalysis (ERA-Interim). To evaluate the model performance on meteorology, 2-m air temperature (T2), 2-m dew point temperature, 10-m wind speed (U10), and wind fields at 500 hPa with a horizontal resolution of  $0.05^{\circ} \times 0.05^{\circ}$  are also obtained from ERA-Interim. It should be noted that 2-m relative humidity (RH2) used to validate the model performance is calculated by 2-m dew point temperature and T2.

### *2.1.2 AERONET*

The identification of aerosol pollution events on the TP is based on quality-assured data from the Aerosol Robotic Network (AERONET), which was established by the U.S. National Aeronautics and Space Administration (NASA) (Holben et al., 1998) and is used to retrieve aerosol properties via sun photometers (Dubovik and King, 2000). AERONET data, including instantaneous data and daily average by calculating the diurnal average of the instantaneous values (Holben et al., 1998), are available at three levels: level 1.0 (unscreened), level 1.5 (cloud-screened), and level 2.0 (cloud-screened and quality assured data) (Smirnov et al., 2009). In this paper, the aerosol optical depth (AOD) and fine-mode AOD at a standard wavelength of 500 nm used to define the aerosol pollution event are based on the Spectral Deconvolution Algorithm (SDA) version 3, level 2.0 (O'Neill et al., 2003; O'Neill et al., 2008). In addition, this kind of AOD data was also used to verify the model performance on the temporal variation of AOD at different sites over the study area.

### 2.1.3 MODIS

The Moderate Resolution Imaging Spectroradiometer (MODIS) instrument aboard the Terra and Aqua satellites is designed with 36 spectral bands ranging from 0.4 to 15  $\mu\text{m}$  and a high spatial resolution for retrieving reliable and extensive information about solar radiation, atmosphere, ocean, cryosphere, and land. The enhanced Deep Blue aerosol retrieval algorithm has substantially improved the collection of 6 aerosol products over the entire land region, especially in deserts and urban regions (Hsu et al., 2013). Herein, to verify the model performance on the spatial distribution of AOD, the AODs based on the Deep Blue algorithm at 550 nm with a horizontal resolution of  $1^\circ \times 1^\circ$  and a daily temporal resolution from MODIS/Aqua Level-3 collection 6 products during the period from April 20 to May 10, 2016 are used. It should be noted that MODIS onboard the Aqua satellite passes over the equator at 13:30 local time.

### 2.1.4 MERRA-2

The second Modern-Era Retrospective analysis for Research and Applications (MERRA-2), which is introduced to replace the original MERRA reanalysis because of the advances in the Goddard Earth Observing System Model, Version 5 (GEOS-5) data assimilation system, is a NASA atmospheric reanalysis, beginning in 1980 (Gelaro et al., 2017). MERRA-2 is the first long-term global reanalysis to assimilate space-based observations of aerosols, including assimilation of AOD retrieved from the Advanced Very High-Resolution Radiometer instrument over the oceans (Heidinger et al., 2014),



the MODIS (Levy et al., 2010), non-bias-corrected AOD retrieved from the Multiangle Imaging SpectroRadiometer (Kahn et al., 2005) over bright surfaces, and ground-based AERONET observations (Holben et al., 1998). This dataset includes all the processes of aerosol transport, deposition, microphysics, and radiative forcing and has considerable skill in showing numerous observable aerosol properties (Gelaro et al., 2017; Randles et al., 2017), including dust, sulfate, organic carbon, BC, and sea salt aerosols (Chin et al., 2002; Colarco et al., 2010). As the first long-term aerosol reanalysis dataset, MERRA-2 has been adequately evaluated in previous studies (Buchard et al., 2017; Che et al., 2019; Sun et al., 2019). In this paper, the hourly surface BC concentration ( $\text{kg/m}^3$ ), which has a spatial resolution of a longitude-by-latitude grid of approximately  $0.625^\circ \times 0.5^\circ$ , is used to validate the model performance on BC. In addition, AOD from MERRA-2 combined with that from MODIS are used to validate the model performance on chemistry.

## *2.2 Definition of an aerosol pollution event*

The two main reference sites used in this study are Nam Co Monitoring and Research Station for Multisphere Interactions (Nam Co), situated in inland TP ( $30.77^\circ \text{N}$ ,  $90.96^\circ \text{E}$ , 4730 m a.s.l.), and Qomolangma Station for Atmospheric and Environmental Observation and Research (QOMS,  $28.36^\circ \text{N}$ ,  $86.95^\circ \text{E}$ , 4276 m a.s.l.), located on the northern slope of Mt. Everest in the central Himalayas. The Nam Co and QOMS stations joined the AERONET network in 2006 and 2009, respectively, and are continuously functioning up to date. Both stations are background stations with fewer human activities and can be regarded as representative sites for the inland of the TP and

the southern TP, respectively (Pokharel et al., 2019). Figure S1 in the supporting information (SI) shows the daily mean of AOD at a standard wavelength of 500 nm lying above the 95th percentile at Nam Co and QOMS stations since 2006 and 2009, respectively. As can be seen, the observed most severe aerosol pollution event ever recorded in the remote TP occurred during the period from April 27 to May 4, 2016, persisting for at least eight days simultaneously at Nam Co and QOMS sites. Figure 1 presents the temporal variation in daily mean AOD and fine-mode AOD at 500 nm for both stations during the period from April 20 to May 10, 2016. Notably, the changes in daily mean AOD and fine-mode AOD are synchronized and the value of daily mean fine-mode AOD is very close to that of daily mean AOD, indicating that the fine particulate matter dominated this severe aerosol pollution event. Meanwhile, it is also acquired from Figure 1 that the most polluted period during this pollution event is from April 27 to May 4. Specifically, at Nam Co station, the observed highest daily mean AOD and fine-mode AOD with values of 0.65 and 0.64 appeared on April 29, 2016; while at QOMS station, the measured highest daily mean AOD and fine-mode AOD with values of 0.42 and 0.39 occurred on May 1, 2016. According to the previous study, the baseline values of AOD at Nam Co and QOMS are 0.029 and 0.027, respectively (Pokharel et al., 2019). Thus, the observed highest AOD at Nam Co and QOMS stations during this severe aerosol pollution event is at least one order of magnitude than that of baseline.

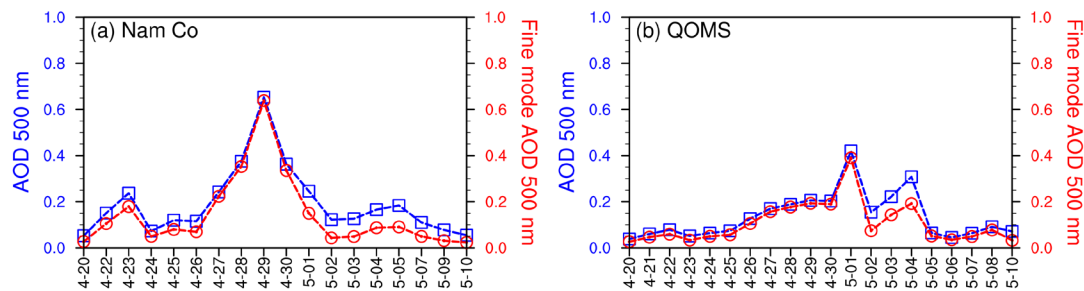


Figure 1. Time series of daily mean AOD (blue) and fine-mode AOD (red) at 500 nm at Nam Co (a) and QOMS (b) stations during the period from April 20 to May 10, 2016.

### 2.3 WRF-Chem model configuration, Emissions, and Experimental design

The WRF-Chem model is a fully coupled regional dynamical/chemical transport model that considers gas-phase chemistry, photolysis, and aerosol mechanism (Grell et al., 2005). The model can simulate the emission, transport, mixing, chemical reactions, and deposition of trace gases and aerosol simultaneously with the meteorological fields. It has been successfully applied in air pollution studies over the TP and adjacent regions (Yang et al., 2018; Chen et al., 2018; Hu et al., 2022). The version used in this study is based on v3.9.1. As shown in Figure 2, the simulation domain is centered at 31°N, 87.5 °E, covering the whole TP and its surroundings. The model simulations are conducted at a 15-km horizontal resolution using a Lambert conformal mapping with 259 (west-east)  $\times$  179 (north-south) grid cells. There are 30 vertical sigma levels for all grids, extending from the surface to 50 hPa. The key physical parameterization options used in this study include the Noah land surface model (Ek et al., 2003; Chen et al., 2010) and the Monin-Obukhov scheme for the surface layer physical processes (Srivastava and Sharan, 2017), the double-moment Morrison microphysical

parameterization (Morrison et al., 2009) with the Grell-Freitas (GF) cumulus scheme (Grell and Freitas, 2014), the Mellor-Yamada-Janjic (MYJ) planetary boundary layer scheme with local vertical mixing (Janjić, 1994), and the Rapid Radiative Transfer Model for General circulation models (RRTMG) coupled with the aerosol radiative effect for both longwave and shortwave radiation (Iacono et al., 2008). With respect to the chemical parameterization options, the Carbon-Bond Mechanism version Z (CBMZ) gas-phase chemistry mechanism (Zaveri and Peters, 1999) combined with the Model for Simulating Aerosol Interactions and Chemistry (MOSAIC) aerosol module (Zaveri et al., 2008) was chosen for aerosol simulation. The MOSAIC aerosol scheme uses an approach of segmentation to represent aerosol size distribution with four or eight discrete size bins (Fast et al., 2006). In this paper, the aerosol size is divided into four bins. Aerosol species simulated by the MOSAIC scheme include sulfate, methanesulfonate, nitrate, chloride, carbonate, ammonium, sodium, calcium, BC, primary organic mass, liquid water, and other inorganic mass.

The initial and boundary conditions for meteorological fields are obtained from the National Centers for Environmental Prediction (NCEP) Final Analysis (FNL) data with a  $1^\circ \times 1^\circ$  spatial resolution and a 6-h temporal resolution (<https://rda.ucar.edu/datasets/ds083.2/>). Anthropogenic emissions, such as CO, VOCs, NO<sub>x</sub>, NH<sub>3</sub>, BC, OC, SO<sub>2</sub>, PM<sub>2.5</sub>, and PM<sub>10</sub>, are taken from the Emission Database for Global Atmospheric Research (EDGAR)-Hemispheric Transport Air Pollution version 2 (HTAPv2) emission inventory ([https://edgar.jrc.ec.europa.eu/dataset\\_htap\\_v2](https://edgar.jrc.ec.europa.eu/dataset_htap_v2)) for the year 2010. Detailed information on the HTAP inventory can be found in Janssens-

Maenhout et al. (2015). The biogenic emissions are based on the Model of Emissions of Gases and Aerosols from Nature (MEGAN) (Guenther et al., 2006; Guenther et al., 2012), and the biomass burning emissions were calculated with the high-resolution fire emissions based on the Fire INventory from NCAR (FINN) (Wiedinmyer et al., 2011). In addition, the mozbc utility and the Community Atmosphere Model with Chemistry (CAM-Chem) (Buchholz et al., 2019) dataset are used to create improved chemical initial and boundary conditions. The simulation is conducted from April 10, 2016 to May 10, 2016, and the first ten days are used for model spin-up. The results from April 20, 2016 to May 10, 2016 are used for the analysis.

There are two experiments involved in this study, one is the control experiment (CONT) and the other is the sensitive experiment (SEN). In the CONT, the simulation is conducted using the WRF-Chem model with aerosol-meteorology feedback turned on. The SEN is exactly the same as CONT except that the feedback between aerosol and meteorology is turned off. The difference between CONT and SEN is considered as the effect induced by aerosol-meteorology feedback.

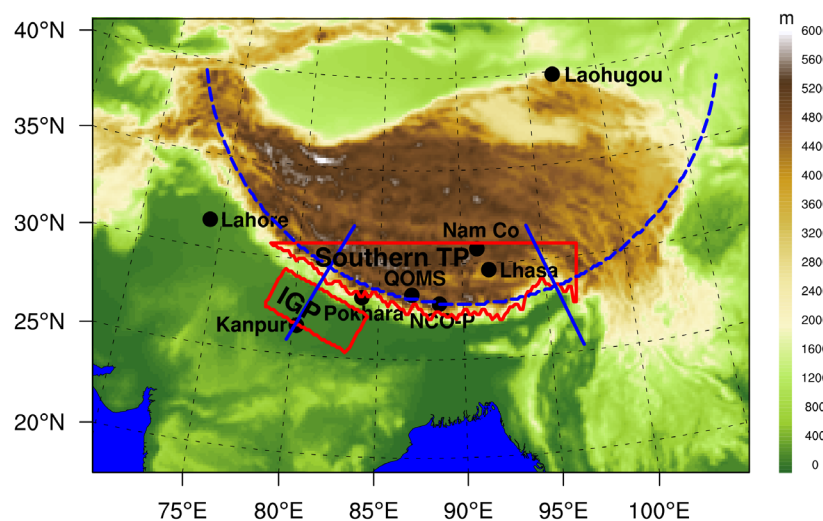


Figure 2. WRF-Chem model domain and terrain (shading; m). Black solid dots denote

stations used to verify model performance on meteorological conditions and aerosols. The solid red lines and its inner area denote the southern TP and Indo-Gangetic Plain. The blue dashed line and two solid lines represent the cross sections for analysis in the following.

## **3 Results and discussion**

### *3.1 Meteorological causes of the severe aerosol pollution event*

Excessive emissions and adverse meteorological conditions are the two most important factors influencing air quality (Wang et al., 2019; Chen et al., 2019b; Liu et al., 2017; Zhang et al., 2019). The TP, which has a small population density and a low degree of industrialization, is one of the most pristine regions on the earth. Moreover, as mentioned above, from April 27 to May 4, 2016, AOD at background stations of Nam Co and QOMS with fewer human activities is significantly higher than that of baseline with the highest value at least one order of magnitude than that of baseline. Therefore, it can be inferred that aerosols over the TP during this severe aerosol pollution event are mainly sourced from adjacent regions by long-range transport, which is consistent with the results reported in a previous study (Kang et al., 2019b). Atmospheric circulation, as the main driving force of atmospheric aerosols, plays a substantial role in the long-range transport of aerosols. Therefore, with little change in emission source, analyzing the meteorological conditions during a severe pollution event is very crucial. Figure 3 shows weather maps at 500 hPa based on the ERA-Interim reanalysis dataset. It is found that, during 08:00–14:00 Beijing Time (hereafter

BJT) on April 27, straight westerly airflow prevailed at 500 hPa over the TP (Figure 3a), which transported aerosols from northwestern South Asia to the TP. Subsequently, wind field shear occurred over the plateau at 20:00 on April 27 (Figure 3b), and plateau vortex generated at 02:00 on April 28 (Figure 3c), which is conducive to the accumulation of aerosols in the inland of the plateau. From 08:00 on April 28 to 08:00 on April 29, the plateau vortex stabilized over the TP, and the aerosol concentrations at Nam Co station continued increasing (figure not shown). At 14:00 on April 29, the plateau vortex disappeared (Figure 3d) and the aerosol concentrations peaked at Nam Co station. Meanwhile, a high-pressure system was located on the west side of the plateau accompanied by a trough on the foreside (Figure 3d). Thus, southwesterly airflow in front of the trough transported aerosols from northern South Asia to the southern TP (Figure 3e). As a result, the aerosol concentrations at QOMS station increased and peaked on May 1. At 14:00 on May 1, the high-pressure system moved eastward from the west side to the inland of the TP and northerly winds ahead of this high-pressure system prevailed over the TP (Figure 3f), which wafted aerosols away from the TP and aerosol concentrations at QOMS station began to decrease.

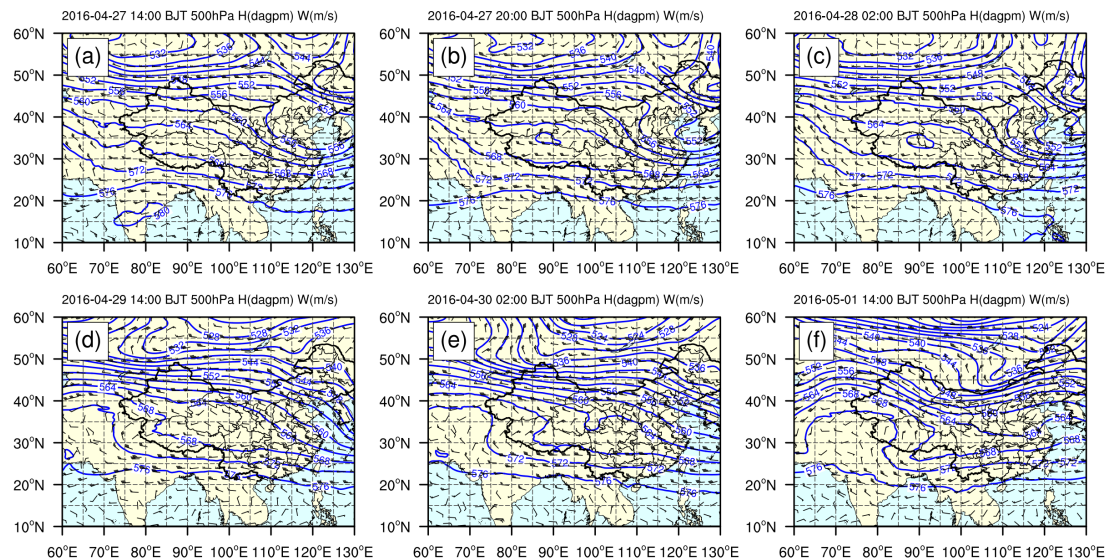


Figure 3. Weather maps at 500 hPa over the study area during the severe aerosol pollution event based on the ERA-Interim reanalysis dataset. The blue lines are isopleths of geopotential height (unit: dagpm). Wind speed (unit: m/s) and direction are denoted by wind barb.

### 3.2 Evaluating model performance on meteorology and chemistry

#### 3.2.1 Validation of model performance on meteorology

Validating model performance on meteorology is critical for assuring accuracy in simulating aerosol concentrations. This is because meteorological conditions are closely associated with aerosol growth, transport, and deposition. Herein, to validate the model performance on meteorological conditions, the temporal variation in the simulated and reanalyzed T2, RH2, and U10 at Nam Co, QOMS, Kanpur, and Lahore stations are shown in Figure S2 in the SI. The model reasonably represents the correct temporal trend of T2 at four stations although underestimations are detected at Nam Co and QOMS stations. The variation trend of RH2 from the simulation is in high



327 consistent with that from reanalysis at Kanpur and Lahore stations. However, at Nam  
 328 Co and QOMS stations, a relatively larger discrepancy is observed between simulation  
 329 and reanalysis, which might be related to the high altitude and complex topography  
 330 there. For U10, the simulated trend on average coincides with the observed trend at  
 331 Nam Co, Kanpur, and Lahore stations. The corresponding statistics, including sample  
 332 size (N), observed mean, simulated mean, mean bias (MB), normalized mean bias  
 333 (NMB), root mean square error (RMSE), and correlation coefficient (R) between  
 334 observation and simulation at different stations are shown in Table S1 in the SI. The  
 335 calculations indicate that T2 is well simulated with MB of  $-4.25$ ,  $-3.62$ ,  $0.03$ , and  $0.07$ ,  
 336 and R of  $0.69$ ,  $0.87$ ,  $0.94$ , and  $0.96$  at Nam Co, QOMS, Kanpur, and Lahore stations,  
 337 respectively. RH2 and U10 are less well simulated, especially at Nam Co and QOMS  
 338 stations, where the altitude is very high and the terrain is fairly complex. To be exact,  
 339 RH2 with MB of  $29.68$  and  $-25.82$  and R of  $0.51$  and  $0.52$  are obtained at Nam Co and  
 340 QOMS stations, respectively. And U10 with MB of  $0.91$  and  $5.66$  and R of  $0.30$  and  
 341  $0.55$  are detected at two stations accordingly. However, at Kanpur and Lahore stations,  
 342 RH2 and U10 from reanalysis and simulation are in high consistency, with MBs of  
 343  $-12.56$  and  $0.85$ ,  $-13.00$  and  $0.96$ , Rs of  $0.80$  and  $0.45$ ,  $0.78$  and  $0.22$ , respectively. As  
 344 a whole, U10 is on average overestimated at four stations and has a greater range of  
 345 about  $3.43$ – $8.56$  m/s compared to reanalyzed values with a range of about  $2.47$ – $3.39$   
 346 m/s. Hence, the simulations are biased at least in part since the model grid represents a  
 347 regional average at  $15 \times 15 \text{ km}^2$  in a domain of great topographic complexity, and the  
 348 values derived from reanalysis with a horizontal resolution of  $0.05^\circ \times 0.05^\circ$  represent a

regional average of a relatively higher resolution. In addition, the accuracy of the gridded observational data of ERA-interim is correlated with the restriction of the observations assimilated into the reanalysis and with the different assimilation methods (Chung et al., 2013). Overall, we conclude that the WRF-Chem model exhibits acceptable performance in simulating temporal variations in meteorological elements.

The spatial distributions of T2, RH2, and wind field at 500 hPa from simulation and reanalysis over the domain are presented in Figure S3 in the SI. Spatially, both simulation and reanalysis show similar spatial patterns for each of the above-mentioned meteorological fields. Exactly, surface air temperature with high values mainly appears over regions surrounding the TP, especially obvious over South Asia where surface air temperature exceeds 30 °C. Previous studies indicated that surface air temperature over the Indian subcontinent is the highest during the pre-monsoon season because the Himalayas block the frigid katabatic winds flowing down from Central Asia during this period (Ji et al., 2011). In contrast, surface air temperature with low values mainly occurs over the TP. Different from T2, RH2 with high values primarily appears over the TP, the Bay of Bengal, and central and eastern China but with low values in the rest area of the domain. Particularly, RH2 in the southeastern TP is apparently higher than that of the inland of the TP, because the southeastern TP is in proximity to the moisture sourced from the Bay of Bengal. Moreover, the reason why the spatial distribution of T2 is antiphase with that of RH2 is that the decrease in T2 can lead to a decrease in the saturation pressure of water vapor and an increase in RH2 at the surface (Gao et al., 2015). With respect to the 500 hPa wind field, both simulation and observation show

that the westerly winds prevail over the entire region. Due to the high topography of the TP, such westerly winds are divided into two branches at appropriate 75 °E. One branch flow eastward, and the other branch is forced up by the high plateau and subsequently shifts to the northwesterly wind. Therefore, the WRF-Chem model also effectively simulates the spatial distributions of T2, RH2, and 500 hPa wind fields. Overall, this simulation configuration captures the meteorological fields well, which is critical to assure simulation accuracy of air pollutant concentrations.

### *3.2.2 Validation of model performance on AOD and BC*

To validate the model performance on simulating spatiotemporal variations in aerosols, ground-based AOD from AERONET together with reanalyzed AOD from MERRA-2 is compared to simulated AOD first. Figure S4 shows the temporal variations in simulated and observed daily mean AOD at Nam Co, QOMS, and Pokhara stations for the period from April 20 to May 10, 2016. As a whole, the WRF-Chem model reasonably reproduces the temporal variations in AOD at each of the above stations, with a relatively larger bias at Nam Co and Pokhara stations and a smaller bias at QOMS station. The specific statistics for N, observed mean, simulated mean, MB, NMB, RMSE, and R between observed and simulated AOD at different stations are shown in Table S2 in the SI. As we note that one-third of AOD values at the selected stations in the MERRA-2 dataset during the study period is missing, the statistical description between the reanalyzed and simulated AOD is not presented. The results from Table S2 indicate that MB with values of -0.13, -0.01, and -0.57, and R with values of 0.58, 0.42, and 0.56 are obtained at Nam Co, QOMS, and Pokhara,

respectively. Moreover, AOD from observation is significantly correlated with that from the simulation at Nam Co and Pokhara stations, with the correlation coefficient passing the 95% confidence level. In addition, we note that the AOD from the simulation is on average lower than that from observation, which may be due to the assumed spherical aerosol particles in the model simulation. The optical properties of particles are more sensitive to non-spherical morphology than primary spherical structure (China et al., 2015;He et al., 2015). On the whole, the model effectively reproduces the observed temporal variation in AOD.

Spatially, the spatial pattern of simulated AOD is in consistent with that from either MODIS or MERRA-2 reanalysis dataset, suggesting a reliable performance of WRF-Chem on simulating AOD. Specifically, AOD from simulation, MODIS, and MERRA-2 shows distinct spatial distribution characteristics, with high values in northern South Asia, the Bay of Bengal, Southeast Asia, and the Sichuan Basin and low values over the TP (Figure S5). This is because northern South Asia, Southeast Asia, and the Sichuan Basin are heavily industrialized and densely populated regions compared to the TP (Bran and Srivastava, 2017). In the Taklimakan Desert, AOD monitored by satellite is much higher than that obtained from simulation, which is likely due to the uncertainty of the emission inventory. Taken together, the comparison between simulation from WRF-Chem and observation from AERONET, MODIS, and MERRA-2 shows that the WRF-Chem model captures the overall spatio-temporal characteristics of AOD over the domain.

To verify the capability of this framework of WRF-Chem on simulating BC

concentration, we present the temporal variation in simulated and reanalyzed hourly BC concentration at Nam Co, QOMS, Lhasa, NCO-P, Laohugou, and Kanpur stations during the period from April 20 to May 10, 2016, as shown in Figure 4. It is found that the WRF-Chem model overall reproduces the temporal variation in reanalyzed BC concentrations at different stations. The specific statistics for N, observed mean, simulated mean, MB, NMB, RMSE, and R between reanalyzed and simulated BC concentrations at different stations are shown in Table S2 in the SI. As can be seen, MB with values of -0.07, 0.14, -0.02, -0.02, 0.02, and 0.72, and R with values of 0.67, 0.43, 0.47, 0.50, 0.25, and 0.64 are obtained at Nam Co, QOMS, Lhasa, NCO-P, Laohugou, and Kanpur stations, respectively. The BC concentrations from the simulation are strongly correlated with those from reanalysis at each of the stations, with a correlation coefficient exceeding the 99% confidence level. Hence, the WRF-Chem model exhibits a better performance in simulating BC concentrations.

Figure S6 presents the spatial distributions of simulated and reanalyzed BC concentrations over the domain. It can be found that BC concentrations from both simulation and reanalysis display distinct spatial variability, with low concentrations over the TP and high concentrations over the north of South Asia, Southeast Asia, and the Sichuan Basin. As one of the most pristine regions on the earth, the TP has a small population density and a low degree of industrialization, resulting in low BC concentrations. Nonetheless, regions adjacent to the TP like north of South Asia, Southeast Asia, and the Sichuan Basin with low elevations have dense populations and developed industrialization (Li et al., 2016a; Qin and Xie, 2012; Li et al., 2016b),

emitting large amounts of BC into the atmosphere and resulting in high BC concentrations. Therefore, the WRF-Chem model can capture the main temporal and spatial features of BC concentrations over the TP and adjacent regions.

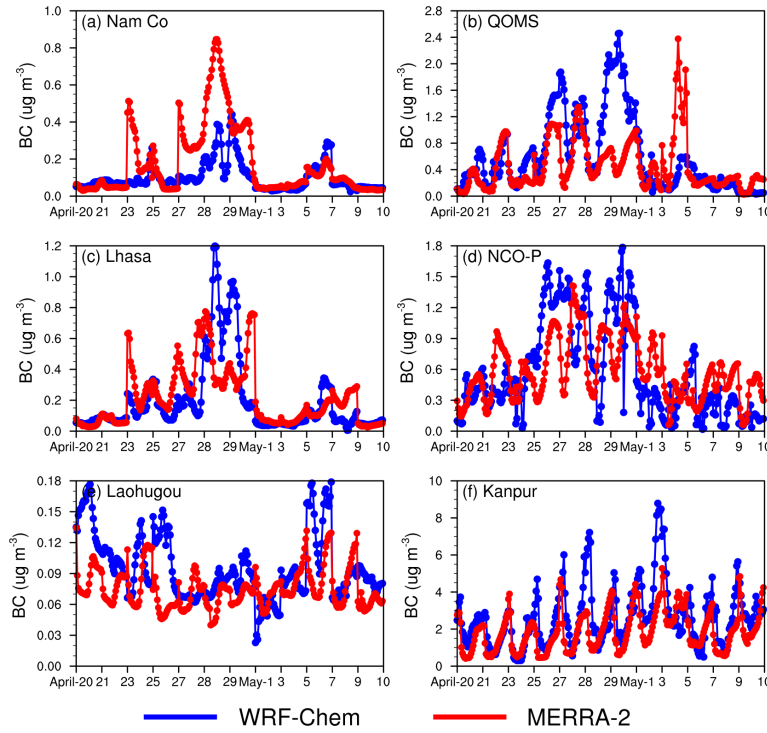


Figure 4. Temporal variations in simulated and reanalyzed hourly BC concentrations at Nam Co (a), QOMS (b), Lhasa (c), NCO-P (d), Laohugou (e), and Kanpur (f) stations for the period from April 20 to May 10, 2016.

### 3.3 Trans-boundary transport flux of BC

The foregoing analysis has validated the model framework used in this study and the results are basically satisfactory. BC, as the major component of light-absorbing particles, exerts a significant impact on climatic and cryospheric changes over the TP due to its strong light absorption and important effect on snow and ice albedo (Kang et al., 2010; Kang et al., 2019b; Yang et al., 2018). In this section, the trans-boundary

transport flux of BC during this severe aerosol pollution event is investigated. According to a previous study, the BC transport flux can be calculated by projecting the wind field perpendicularly to the cross line and then multiplying the BC mass concentration along the cross line (Zhang et al., 2020). More specifically, the BC transport flux is calculated as follows:

$$TF = C \cdot (u \cdot \sin \alpha + v \cdot \sin \beta), \quad (1)$$

where  $\alpha$  is the angle between the east–west wind component and the cross line,  $\beta$  is the angle between the south–north wind component and the cross line, and  $C$  is the BC mass concentration at the grid along the cross line. The flux is estimated at each model level. Positive values represent the transport towards the TP, while negative values represent the transport away from the TP. Figure 5 presents the longitude-height cross section of BC transport flux along the cross line (shown as the blue dashed lines in Figure 2) from the simulation with aerosol-meteorology feedback at 15:00 and 03:00 BJT averaged for the period from April 27 to May 4 (the most polluted period) to represent daytime and nighttime transport, respectively. Notably, in the central and western Himalayas (to the west of  $\sim 94^\circ\text{E}$ ), BC is imported into the TP during both day and night times, especially obvious at the height of below 7 km, although the transport flux during the nighttime is higher than that during the daytime. In the eastern Himalayas (from  $94\text{--}98^\circ\text{E}$ ), BC is imported into the TP during the day but exported slightly from the TP during the night. To the east of  $\sim 98^\circ\text{E}$ , BC is transported away from the TP during the day and night due to the prevailed westerly winds. Generally, the transport across the western Himalayas is controlled by the large-scale westerly,

while the transport across the central and eastern Himalayas is primarily dominated by a local southerly (Zhang et al., 2020). Therefore, the difference in BC transport flux between the western and eastern Himalayas is attributed to the influence of a large-scale westerly that is weak over the eastern Himalayas. The stronger diurnal variation of local southerly (towards the TP in the daytime to away from the TP in the nighttime) compared to that of a westerly near the surface leads to the large difference in diurnal variation of the transport between the western and eastern Himalayas. In addition, the largest BC transport flux along the cross line occurs at deeper mountain valley channels (Figure 5). Zhang et al. (2020) investigated the impact of topography on BC transport to the southern TP during the pre-monsoon season and found that the BC transport across the Himalayas could overcome the majority of mountain ridges, but the valley transport is more efficient, which is consistent with the results obtained in this study.

As the largest BC transport flux occurs at deeper mountain valleys, the two deepest mountain valley channels along the cross line shown as the blue solid line in Figure 2 are selected to demonstrate the BC transport flux across mountain valleys during this severe pollution event. The first valley (referred to as valley-1 hereon) is located in the southwestern TP, while the second valley (referred to as valley-2 hereon) is located in the southeastern TP. It is seen that, at valley-1, the overall positive values near the surface indicate that BC is imported into the TP during the daytime and nighttime, though the transport flux at night is much higher than that during the daytime (Figure 5). Averaged BC concentration and transport flux at 03:00 and 15:00 BJT during the period from April 27 to May 4, 2016 across valley-1 from the simulation with aerosol-



495 meteorology feedback also shows that the BC transport flux is much higher during the  
496 night than that during the daytime (Figure 6a–b). By checking the surface BC  
497 concentration from simulation with aerosol-meteorology feedback, it is found that the  
498 surface BC concentration at valley-1 during the night is much higher than that during  
499 the daytime (Table 1). Moreover, the vertically integrated BC concentration over the  
500 Himalayas is much higher in the nighttime than that in the daytime (Figure S7). With  
501 the help of the large westerly winds, BC then is transported to the TP, which further  
502 provides evidence for the higher BC transport flux during the night shown in Figure 6b.  
503 At valley-2, the near-surface positive flux values during the daytime and negative  
504 values during the night denote that BC is imported into the TP during the daytime but  
505 exported slightly from the TP at night (Figure 5). To analyze this distinct diurnal  
506 variation in BC transport flux, we present the latitude–height cross section of BC  
507 transport flux and its concentration at 03:00 and 15:00 BJT averaged for the period from  
508 April 27 to May 4, 2016 across valley-2 from the simulation with aerosol-meteorology  
509 feedback as shown in Figure 6c–d. Notably, the deeper PBLH and the strong turbulent  
510 mixing during the daytime over northern India allows BC to be mixed at a higher  
511 altitude (Figure 6c). Subsequently, the local southerlies boost the BC transporting  
512 across the eastern Himalayas towards the TP. Nevertheless, during the night, the  
513 meridional wind is dominated by a northerly over the eastern Himalayan region (Figure  
514 6d), suggesting the cross-Himalayan transport is away from the TP.

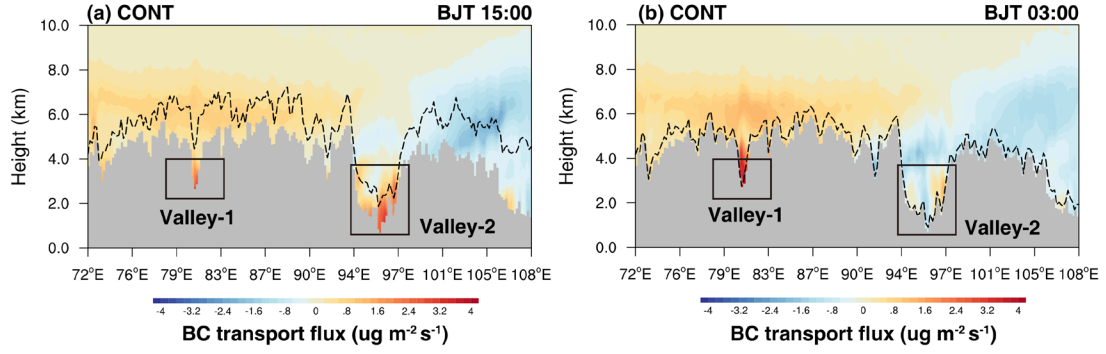


Figure 5. Longitude–height cross section of BC transport flux along the cross line (shown as the blue dashed line in Figure 2) at 15:00 and 03:00 BJT averaged for the period from April 27 to May 4, 2016 from simulation with aerosol-meteorology feedback. The PBLH along the cross section is shown here as the black dashed line.

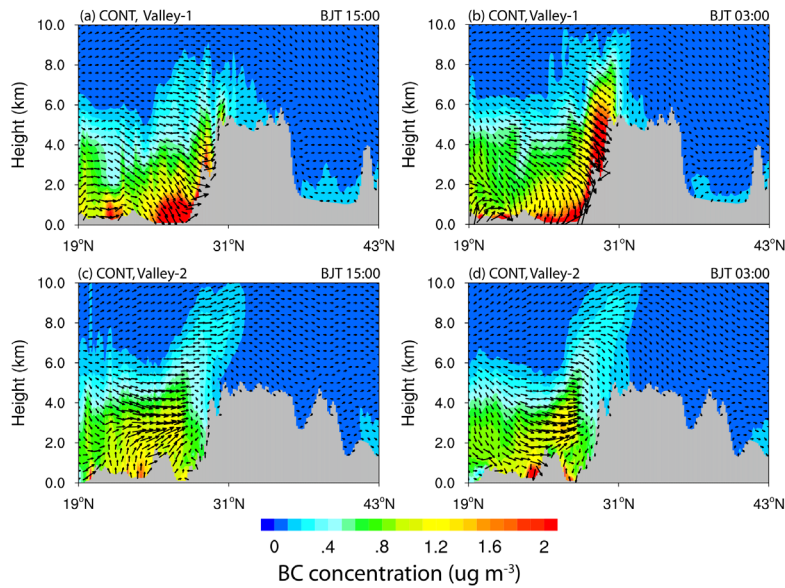


Figure 6. Latitude–height cross section of BC transport flux (vector) across the mountain (a, b) valley-1 and (c, d) valley-2 at 15:00 and 03:00 BJT averaged for the period from April 27 to May 4, 2016 from simulation with aerosol-meteorology feedback. Contour represents the BC concentration.

Table 1. Surface BC concentration at two typical mountain valley channels at 15:00 and 03:00 BJT averaged for the period from April 27 to May 4, 2016 from simulation with aerosol-meteorology feedback.

Near-surface BC concentration	15:00		03:00	
	Valley-1	Valley-2	Valley-1	Valley-2
CONT	1.27	0.75	2.55	0.46

To further demonstrate the overall inflow flux across the Himalayas, the vertically integrated BC mass flux along the longitudinal cross section as shown in Figure 5 from simulation with aerosol-meteorology feedback is shown in Figure 7. The total mass flux is calculated by integrating the right-hand term of Eq. (1) as follows:

$$ITF = \int_{z=z_{sfc}}^{z=z_{top}} \delta z \cdot C \cdot (\mu \cdot \sin\alpha + v \cdot \sin\beta), \quad (2)$$

where  $\delta z$  is the thickness of each vertical model level. Similarly, positive flux values represent the transport towards the TP, while negative values represent the transport away from the TP. It has been found that the positive values primarily exist in the central and western Himalayas (to the west of 92 °E), while negative values mainly exist to the east of 92 °E (Figure 7). Furthermore, the vertically integrated transport flux of BC along the cross line is strongly correlated with the longitudinal degree of the cross line, with the correlation coefficient up to  $-0.89$ , passing the 99% confidence level. This indicates that the vertically integrated transport flux of BC along the cross line decreases from west to east. In particular, from 80 to 86 °E along the cross line, the correlation coefficient between the terrain height and the vertically integrated transport

flux of BC is  $-0.87$ , exceeding the 99% confidence level, suggesting that the lower the valleys are, the higher the vertically integrated transport flux transported across the Himalayas can be. Particularly, the largest vertically integrated transport flux about  $20.8 \text{ mg m}^{-2} \text{ s}^{-1}$  occurs at valley-1. However, to the eastern Himalayas (to the east of  $\sim 92^\circ \text{E}$ ), the BC is overall exported away from the TP and the vertically integrated transport flux with the largest value near to zero occurs at valley-2.

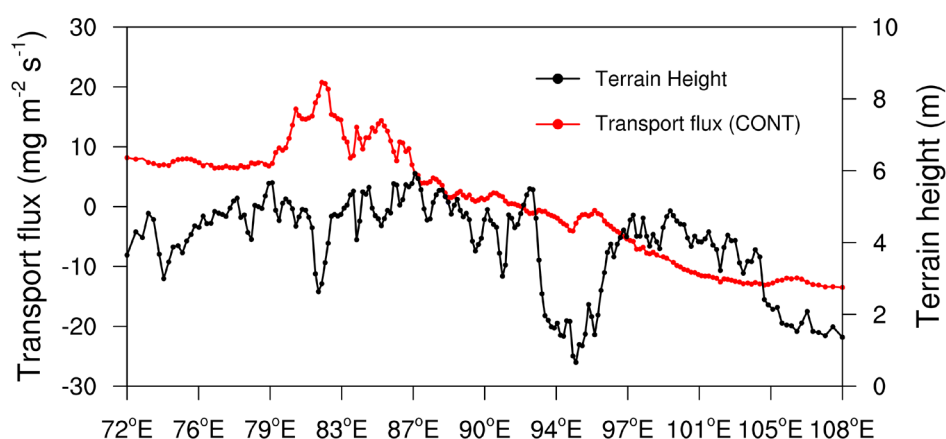


Figure 7. Longitudinal distribution of vertically integrated BC mass flux (red line) along the cross section in Figure 2 from simulation with aerosol-meteorology feedback. The black line represents the terrain height.

### 3.4 Aerosol-meteorology feedback during the severe aerosol pollution event

Generally, the severe aerosol pollution event is accompanied by complex feedback between aerosol and meteorology. The analysis above confirms that BC in northern South Asia can be transported to the TP via the cross-Himalayan transport during this severe pollution event. Moreover, compared to the eastern Himalayas, the western Himalayas contributes more BC to the TP and BC from the cross-Himalayan transport mainly concentrated in the southern TP. Therefore, in this section, the feedback

between aerosol and meteorology over the western Indo-Gangetic Plain (referred to IGP hereon) and southern TP during this severe pollution event is analyzed.

To illustrate the aerosol radiative forcing (ARF) and its impacts on T2, RH2, surface energy, atmospheric stability, wind, and PBLH over the southern TP and IGP regions, the time series of aerosol-induced daily and diurnal changes in meteorological variables (T2, RH2) and surface energy budget (latent heat (LH), sensible heat (SH), shortwave (SW) radiation, longwave (LW) radiation, and net energy flux (LH+LW+SH+SW)) averaged for the southern TP and IGP regions, which is calculated by subtracting the model results of SEN from those of CONT, is shown in Figure 8. It should be noted that the diurnal change is calculated for the most polluted period from April 27 to May 4. As can be seen, the daily variation of aerosol-induced area-averaged surface air temperature ranged from  $-0.1$  to  $0.1$  °C in the southern TP, with a discernable decrease of  $0.1$  °C appearing on May 2, May 4, and May 6–7 (Figure 8a), and from  $-1.7$  to  $1.2$  °C in the IGP (Figure 8c) during the period from April 20 to May 10. During the most polluted period from April 27 to May 4, the aerosol-induced surface air temperature ranged from  $-0.1$  to  $0.1$  °C in the southern TP (Figure 8a), with a decrease of  $0.1$  °C on May 2 and May 4, and decreased by  $0.5$ – $1.7$  °C in the IGP (Figure 8c). The daily variation of aerosol-induced area-averaged RH2 displayed a slight change with values ranging from  $-1.6\%$  to  $2.3\%$  over the southern TP (Figure 8a) and exhibited a greater range of about  $-10.9\%$ – $13.7\%$  in the IGP (Figure 8c) during the period from April 20 to May 10. From April 27 to May 4 with high aerosol concentrations, area-averaged RH2 increased by  $0$ – $2.3\%$  and by  $0.8\%$ – $13.7\%$  in the

southern TP and IGP, respectively (Figure 8a, c). For the diurnal change depicted in Figure 8b and Figure 8d, during 09:00–20:00 BJT in the daytime, the aerosol-induced area-averaged surface air temperature had a range of about  $-0.1$ – $0.1$  °C in the southern TP and decreased by  $0.9$ – $2.3$  °C in the IGP. At night, surface air temperature increased by  $0.1$  °C during 00:00–05:00 BJT in the southern TP (Figure 8b), and decreased by  $0$ – $1.0$  °C during 21:00–08:00 BJT in the IGP (Figure 8d). The corresponding diurnal change in aerosol-induced RH2 indicated that the aerosol-induced RH2 decreased by  $0.1\%$ – $0.4\%$  during 14:00–17:00 BJT in the southern TP but increased during the rest time of the day, with the maximum increase of  $1.3\%$  occurring during 09:00–10:00 BJT (Figure 8b). In the IGP, the aerosol-induced RH2 increased by  $3.3\%$ – $7.1\%$  during 09:00–20:00 BJT in the daytime and increased by  $2.6\%$ – $4.5\%$  during 21:00–08:00 in the nighttime (Figure 8d). Therefore, the aerosol-induced changes in T2 and RH2 primarily occur in the daytime.

Generally, surface energy with positive values indicates more energy flux toward the surface, and vice versa. Figure 8e–h shows the aerosol-induced surface energy changes over the southern TP and IGP, it is found that the SW radiation flux at the surface decreased by  $0$ – $13.7$   $\text{Wm}^{-2}$  in the southern TP (Figure 8e) and by  $44.5$ – $75.3$   $\text{Wm}^{-2}$  in the IGP (Figure 8g) during the period from April 27 to May 4 due to absorbing and scattering solar radiation by aerosol. In contrast, LW radiation flux at the surface of southern TP and IGP increased due to the positive radiative forcing of aerosol in the atmosphere, with an increase of  $4.1$ – $4.6$   $\text{Wm}^{-2}$  in the southern TP from April 30 to May 1 (Figure 8e) and a large increase of  $12.3$ – $23.4$   $\text{Wm}^{-2}$  in the IGP from April 27 to May

4 (Figure 8g). Because of the aerosol's radiative cooling effects, the LH and SH fluxes from the surface to the atmosphere in both regions decreased. Particularly, in the southern TP, the LH and SH fluxes with the maximum decreases of  $2.0 \text{ Wm}^{-2}$  and  $7.8 \text{ Wm}^{-2}$  occurred on April 30 and April 29, respectively (Figure 8e). In the IGP, the LH and SH fluxes, respectively, decreased by  $4.1\text{--}7.4 \text{ Wm}^{-2}$  and by  $26.6\text{--}43.6 \text{ Wm}^{-2}$  from April 27 to May 4 (Figure 8g). The net energy flux at the surface decreased by  $1.6\text{--}18.8 \text{ W m}^{-2}$  in the southern TP (Figure 8e) and by  $62.7\text{--}104.3 \text{ Wm}^{-2}$  in the IGP (Figure 8g) from April 27 to May 4. Therefore, the energy arriving at the surface of southern TP and IGP decreased during this severe aerosol pollution event. For the diurnal change of surface energy, during 09:00–20:00 BJT in the southern TP, the SW, LH, SH, and net energy fluxes decreased by  $7.8\text{--}19.9 \text{ Wm}^{-2}$ ,  $0\text{--}2.4 \text{ Wm}^{-2}$ ,  $4.7\text{--}12.2 \text{ Wm}^{-2}$ , and  $13.4\text{--}29 \text{ Wm}^{-2}$ , respectively, while the LW flux increased by  $0.3\text{--}2.9 \text{ Wm}^{-2}$  (Figure 8f). During 09:00–20:00 BJT in the IGP, the SW, LH, SH, and net energy fluxes decreased by  $46.1\text{--}144.2 \text{ Wm}^{-2}$ ,  $7.5\text{--}16.6 \text{ Wm}^{-2}$ ,  $9.6\text{--}100.1 \text{ Wm}^{-2}$ , and  $54.7\text{--}221.5 \text{ Wm}^{-2}$  accordingly, whereas the LW flux increased by  $8.5\text{--}30.5 \text{ Wm}^{-2}$  (Figure 8h). Therefore, changes in surface energy mainly occur during the daytime.

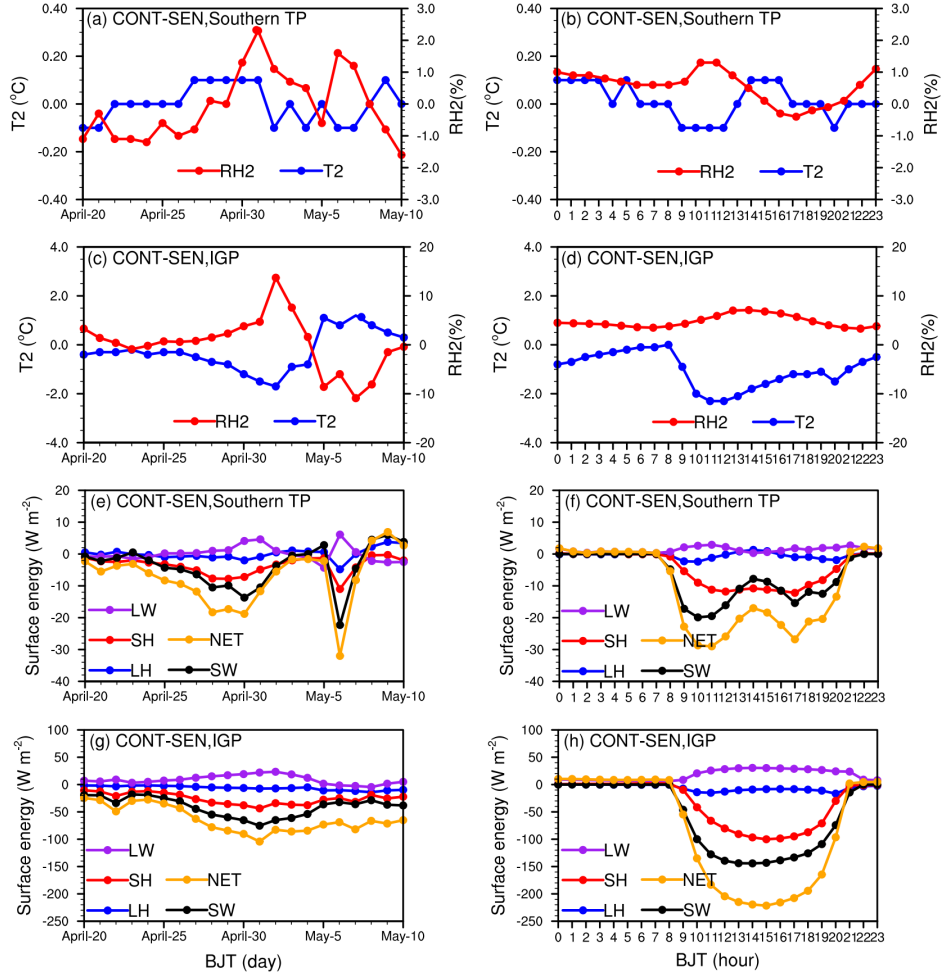


Figure 8. Time series of aerosol-induced daily changes in (a, c) meteorological variables (T2 (°C), RH2 (%)) and (e, g) surface energy budget (SH, LH, LW radiation, SW radiation, and net energy flux,  $\text{Wm}^{-2}$ ) averaged for the (a, e) southern TP and (c, g) IGP during the period from April 20 to May 10. Time series of aerosol-induced diurnal changes in (b, d) meteorological variables and (f, h) surface energy budget averaged for the period from April 27 to May 4, 2016 for the (b, f) southern TP and (d, h) IGP. LH is latent heat, LW is long-wave radiation, SH is sensible heat, SW is shortwave radiation, and NET is the sum of the total energy fluxes.

Figure 9 shows the spatial distribution of aerosol-induced changes in T2 and RH2



and aerosol radiative forcing (ARF) at the bottom of the atmosphere as well as in the atmosphere, calculated by subtracting the model results of SEN from those of CONT averaged during 09:00–20:00 BJT from April 27 to May 4. As seen in Figure 9a, the aerosol-induced surface air temperature decreased over most parts of the study area except for the TP, where surface air temperature increased, especially obvious in the northern TP, with surface air temperature increasing by up to 1.0 °C. Because the TP is one of the most pristine regions on the earth and has fewer human activities, there are significantly less aerosols over the TP compared to the regions surrounding the TP. Consequently, the surface-reaching solar radiation over the TP in the daytime is higher than that of its surroundings, leading to higher surface temperature. A decrease in surface-reaching solar radiation during daytime can lead to a decline in surface air temperature. From Figure 9a, the largest surface air temperature decrease due to aerosols occurred in South Asia since South Asia has large amounts of aerosols due to rapid economic growth, industrialization, and unplanned urbanization compared to other regions (Shi et al., 2020). The spatial distribution of aerosol-induced changes in RH2 is opposite to that of T2, with increased RH2 appearing in most parts of the study area and decreased RH2 on the TP. Specifically, the largest increase in RH2 occurred in northern South Asia, since the aerosol-induced changes in water vapor mixing ratio is very small, and the decrease in temperature can lead to a decrease in the saturation pressure of water vapor and an increase in RH2 at the surface, which is beneficial for the hygroscopic growth of aerosols (Gao et al., 2015). By analyzing the time–altitude distribution of the diurnal cycle of aerosol impacts on temperature and relative humidity

(RH) averaged for the southern TP and IGP during the period from April 27 to May 4, it is found that, consistent with the aerosol-induced changes in T2 and RH2, the aerosol-induced changes in temperature and RH mainly occurred during daytime as well (Figure S8). Specifically, in the southern TP, the maximum increase in temperature with value up to 0.15 °C occurred in the middle troposphere (Figure S8a). However, in the IGP, the temperature decreased near the surface with a maximum drop of more than 0.3 °C and increased in the middle troposphere with a maximum increase of more than 0.3 °C (Figure S8c). There is no doubt that such a temperature change increases the stability of the atmosphere over both regions. Note that the temperature increase in the middle troposphere over the southern TP is more significant than that in the IGP, which is possibly correlated with the thermal pump role of the TP (Li and Yanai, 1996; Meehl, 1994; Yanai et al., 1992). The time–altitude distribution of the diurnal cycle of RH is opposite to that of temperature, with RH increasing near the surface and decreasing in the middle troposphere (Figure S8b and Figure S8d). To be exact, RH decreased by 1.6% in the middle troposphere over the southern TP (Figure S8b), while in the IGP, RH increased near the surface with value greater than 3% and decreased by more than 3% in the middle troposphere (Figure S8d).

The ARF at the bottom of the atmosphere is negative over most parts of the study area except for the northern TP, where ARF is positive, with ARF up to 20 W m<sup>-2</sup> (Figure 9c). The observed largest negative ARF occurred in northern South Asia and the Bay of Bengal, with values in a range of about -40—-120 Wm<sup>-2</sup> (Figure 9c). Contrary to the spatial distribution of ARF at the bottom of the atmosphere, the ARF in

the atmosphere is positive over most parts of the study area, with the largest ARF up to  $110 \text{ Wm}^{-2}$  in South Asia (Figure 9d). Thus, affected by aerosols, the atmospheric stratification over the study area is expected to be more stable.

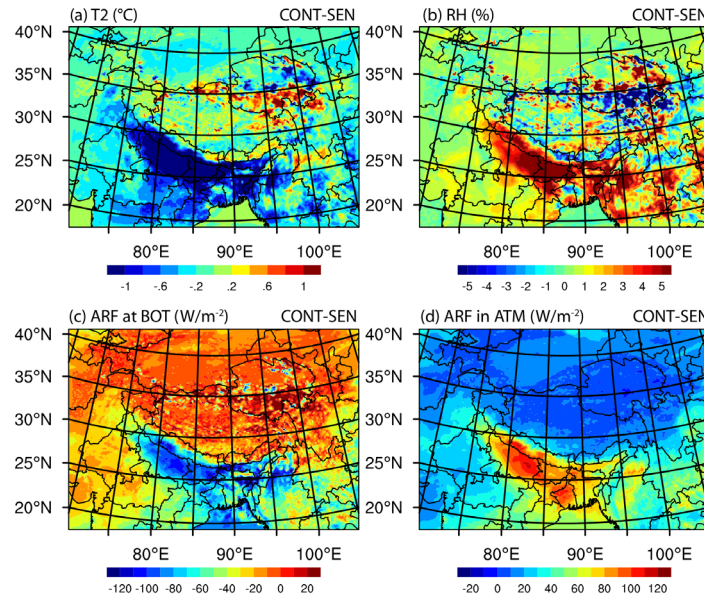


Figure 9. Spatial distribution of aerosol-induced changes in (a) T2 ( $^{\circ}\text{C}$ ) and (b) RH2 (%), and aerosol radiative forcing (ARF,  $\text{Wm}^{-2}$ ) (c) at the bottom of (BOT) and (d) in the atmosphere (ATM) averaged for 09:00–20:00 BJT during the period from April 27 to May 4, 2016.

From the above analysis, the aerosol-induced changes in meteorological conditions and ARF have significant impact on atmospheric stability. The profile of equivalent potential temperature (EPT) can be used to characterize the stability of the atmosphere. Figure S9 in the SI shows the aerosol-induced changes in EPT profiles at 02:00, 08:00, 14:00, and 20:00 BJT averaged during the period from April 27 to May 4 in the southern TP and IGP. It can be seen that aerosol impact on EPT over the southern TP with values in a range of about 0.08–0.24 K is overall smaller than that in

the IGP with values in a range of about  $-1.6$ – $3.2$  K because of low aerosol concentrations in the southern TP and high aerosol concentrations in the IGP. Specifically, at 08:00, 14:00, and 20:00 BJT, the EPT in the southern TP decreased with height in the lower and middle troposphere, and increased with height above the middle troposphere (Figure S9a). However, in the IGP, at 02:00 and 20:00 BJT, the EPT decreased with height below 550 hPa and increased with height above 550 hPa; while at 14:00 BJT, the EPT decreased with height below 650 hPa and increased with height between 650 and 550 hPa (Figure S9b). Therefore, an obvious temperature inversion was detected in the troposphere over the southern TP and IGP during the severe aerosol pollution event.

Under a more stable atmosphere, the diurnal variation of surface BC concentration from control experiment with aerosol-meteorology feedback and the aerosol-induced changes in U10 and planetary boundary layer height (PBLH) over the southern TP and IGP are presented in Figure 10. Overall, the surface BC concentration over the southern TP and IGP was high during 20:00–08:00 BJT in the nighttime but low during 08:00–20:00 BJT in the daytime. Over the southern TP, the aerosol-induced PBLH decreased with value up to 55 m during 09:00–14:00 BJT and by 70 m during 18:00–20:00 BJT, while at other times of the day, no obvious change in PBLH was observed (Figure 10a). In the IGP, the aerosol-induced PBLH decreased during 10:00–20:00 BJT in the daytime, with the largest decrease of 1700 m occurring at 20:00 BJT (Figure 10b). Lower PBLH constrains the pollutants to diffuse in the vertical direction and is conducive to the accumulation of pollutants near the ground. The aerosol-induced U10

increased in the southern TP, with the maximum increase of 0.2 m/s appearing at 19:00 BJT (Figure 10a). In the IGP, the aerosol-induced U10 decreased, with the largest decrease of 0.7 m/s appearing at 20:00 BJT (Figure 10b). Therefore, aerosol induces significant changes in meteorological conditions in the southern TP and IGP during this severe aerosol pollution event.

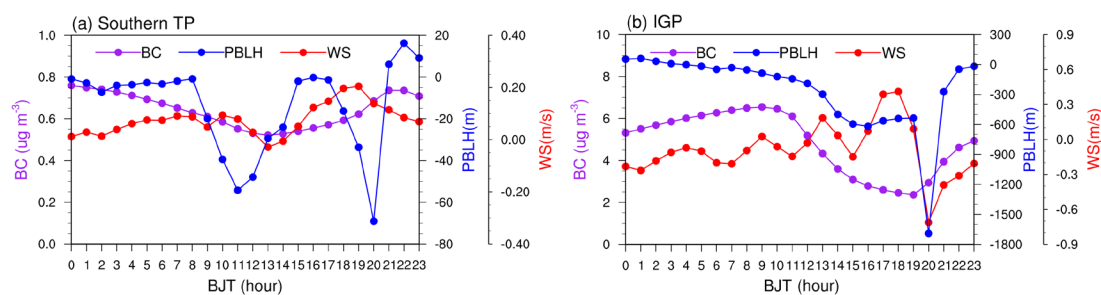


Figure 10. Diurnal variation of surface BC concentration ( $\mu\text{g m}^{-3}$ ) from control experiment with aerosol-meteorology feedback (purple solid line) and aerosol-induced diurnal changes in 10-m wind speed (red solid line, WS,  $\text{m s}^{-1}$ ) and PBLH (blue solid line, m) averaged for (a) the southern TP and (b) IGP during the period from April 27 to May 4, 2016.

The aerosol-induced changes in meteorological conditions have important effect on surface BC concentration, which eventually exerts potential influence on aerosol pollution as well as weather and climate (Menon et al., 2002). Figure 11a and b show the hourly surface BC concentration from sensitive experiment without aerosol-meteorology feedback and the impact of aerosol-induced changes in meteorological variables on hourly surface BC concentration averaged over the southern TP and IGP during the period from April 20 to May 10. The corresponding diurnal cycle during the

most polluted period from April 27 to May 4 are shown in Figure 11c and d. The change  
 in percentage is calculated by comparing with the surface BC concentration from the  
 experiment without aerosol-meteorology feedback. It can be seen that the aerosol-  
 induced changes in meteorological conditions lead to a decrease of surface BC  
 concentration with value up to  $0.16 \mu\text{g}/\text{m}^3$  (50%) in the southern TP. However, in the  
 IGP, the aerosol-induced changes in meteorological conditions result in an increase in  
 surface BC concentration with value up to  $2.2 \mu\text{g}/\text{m}^3$  (75%). Moreover, the higher the  
 surface BC concentration is, the greater the variation in the surface BC concentration  
 induced by meteorological conditions is. It should be noted that the time when the  
 maximum decrease or increase in surface BC concentration occurs is not the time when  
 the maximum surface BC concentration occurs. The diurnal changes in surface BC  
 concentration during the most polluted period from April 27 to May 4 over the southern  
 TP indicate that the surface BC concentration is high during 20:00–07:00 BJT in the  
 nighttime and low during 08:00–19:00 BJT in the daytime, with the lowest  
 concentration of  $0.6 \mu\text{g}/\text{m}^3$  observed at 12:00 BJT. The changes in meteorological  
 conditions lead to a reduction of the surface BC concentration over the southern TP,  
 with the reduction primarily occurring during 11:00–19:00 BJT in the daytime and the  
 largest reduction of  $0.06 \mu\text{g}/\text{m}^3$  (12%) appearing at 15:00 BJT. The corresponding  
 diurnal changes in the IGP reveal that the surface BC concentration is high during  
 23:00–12:00 BJT and low during 13:00–22:00 BJT. The changes in the meteorological  
 conditions result in an increase in the surface BC concentration, with a relatively larger  
 increase of about  $0.7\text{--}1.1 \mu\text{g}/\text{m}^3$  occurring during 20:00–13:00 BJT. Therefore, the

changes in meteorological conditions enhance the diurnal variation of surface BC concentration by decreasing the surface BC concentration in the southern TP and increasing the surface BC concentration in the IGP.

Figure S10 in the SI shows the impact of aerosol-induced changes in meteorological conditions on the spatial distribution of surface BC concentration averaged during 09:00–20:00 BJT, April 27–May 4. Consistent with Figure 11, the maximum increase in surface BC concentration induced by the changes in meteorological conditions occurs in the IGP (northwestern South Asia), with values greater than  $1 \mu\text{g}/\text{m}^3$ . The corresponding surface BC concentration change in percentage terms is also higher in northwestern South Asia with value up to 30%, and is lower in the southeastern TP with value below 30% (Figure S10b). Taken together, aerosols result in significant changes in meteorological conditions in the Southern TP and IGP, with an obvious decrease in PBLH and U10 along with a more stable atmosphere in the IGP, and a decrease in PBLH but an increase in U10 accompanied by a stable atmosphere in the Southern TP. In addition, the aerosol-induced changes in meteorological conditions have substantial influence on surface aerosol concentration. For instance, in the IGP, the changes in meteorological conditions induced by aerosols are conducive to the accumulation of aerosols, thereby contributing to the formation of severe aerosol pollution event. Consequently, a positive feedback mechanism exists between aerosol concentration and aerosol-induced meteorological conditions in the IGP. However, as one of the major source regions of aerosols over the TP, the aerosol-induced changes in meteorological conditions in the IGP are not favorable for aerosols

transporting to the southern TP.

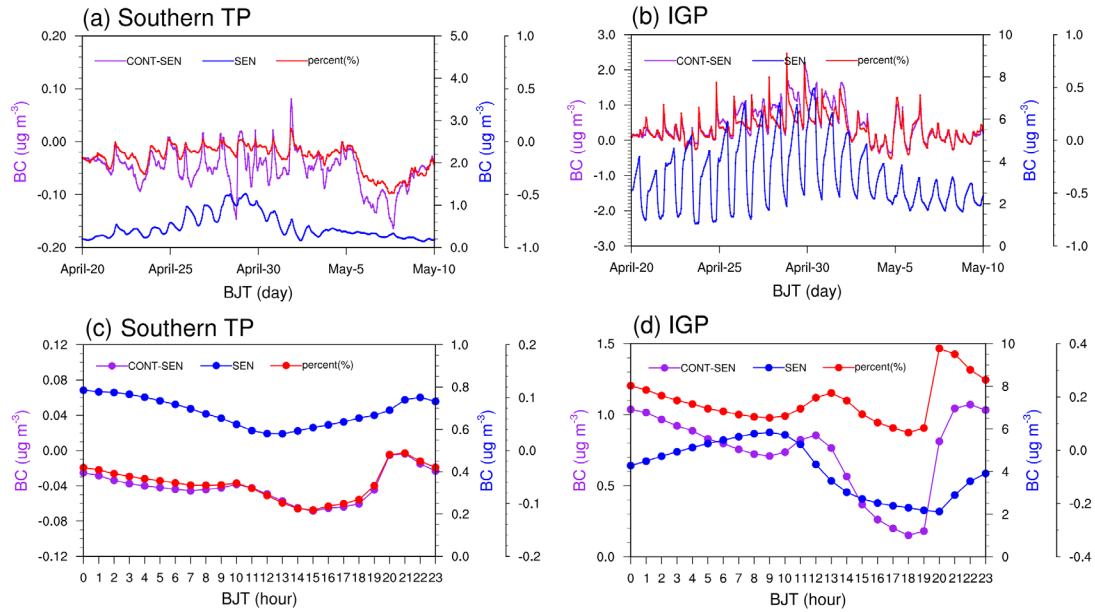


Figure 11. Time series of hourly surface BC concentration from SEN (blue solid line) averaged for (a) the southern TP and (b) the IGP during the period from April 20 to May 10, 2016 and the corresponding diurnal changes (blue solid line) averaged (c) for the southern TP and (d) the IGP during the period from April 27 to May 4, 2016. The purple solid line denotes the change value of surface BC concentration induced by meteorological conditions. The red solid line indicates the corresponding change in percentage terms compared to the surface BC concentration from the model results of SEN.

### 3.5 Impact of aerosol-meteorology feedback on the trans-boundary transport flux of BC

As discussed above, during the severe aerosol pollution event, northwestern South Asia contributes more BC to the TP via cross-Himalayan transport and the largest BC



transport flux occurs at mountain valley in western Himalayas. Moreover, the aerosol-meteorology feedback has substantial effect on surface BC concentration over the southern TP and IGP. Yet what effect the aerosol-meteorology feedback having on the trans-boundary transport flux of BC remains unclear, which deserves further investigation. Therefore, this section is aimed at demonstrating the impact of aerosol-meteorology feedback on the trans-boundary transport flux of BC during the severe aerosol pollution event. Figure 12 shows the difference in longitude–height cross section of BC transport flux along the cross line (shown as the blue dashed line in Figure 2) from the simulations with and without aerosol-meteorology feedback at 15:00 and 03:00 BJT averaged for the period from April 27 to May 4, 2016. It can be seen that, during the daytime, in the central and western Himalayas (75–90 °E), the aerosol-meteorology feedback overall increases the BC transport flux towards the TP at the height of about 6–7 km but decreases the BC transport flux at the height of below 6 km; however, in the eastern Himalayas (90–98 °E), the aerosol-meteorology feedback decreases the BC transport flux exporting from the TP. During the nighttime, from 80 °E to 87 °E in the central Himalayas, the aerosol-meteorology feedback increases the BC transport flux towards the TP at the height of about 6–7 km but decreases the BC transport flux at the height of below 6 km; however, from 87 °E to 94 °E in the eastern Himalayas, the aerosol-meteorology feedback decreases the BC transport flux towards the TP at the height of below 7 km and from 94 °E to 98 °E, the aerosol-meteorology feedback decreases the BC transport flux exporting from the TP.

In addition, by analyzing the impact of aerosol-meteorology feedback on the BC

818 transport flux at two typical mountain valley channels, it is found that, at valley-1, the  
 819 feedback decreases the BC transport flux towards the TP during the daytime and  
 820 nighttime; while at valley-2, the feedback decreases the BC transport flux towards the  
 821 TP during the daytime and reduces the BC transport flux away from the TP during the  
 822 nighttime. To better understand the effect of aerosol-meteorology feedback on the BC  
 823 transport flux at two typical mountain valley channels of valley-1 and valley-2, we  
 824 investigated the mean zonal and meridional wind speeds within 500 m above the ground  
 825 level at both valleys during the daytime and nighttime from April 27 to May 4, 2016  
 826 (Table 2) from simulations with and without aerosol-meteorology feedback. It is found  
 827 that, during the daytime, a westerly and a southerly prevail at valley-1 but an easterly  
 828 and a southerly prevail at valley-2; during the night, an easterly and a northerly prevail  
 829 at both valleys in both experiments. Specifically, at valley-1, the differences in zonal  
 830 and meridional wind speeds between the simulations with and without aerosol-  
 831 meteorology feedback at 15:00 and 03:00 BJT averaged for the period from April 27 to  
 832 May 4, 2016 show that, during the daytime, the aerosol-meteorology feedback overall  
 833 decreases the westerly and southerly wind speeds, resulting in decreased BC transport  
 834 flux towards the TP; during the night, the aerosol-meteorology feedback leads to  
 835 increased easterly and northerly wind speeds, strengthening the BC transport flux being  
 836 away from the TP. The corresponding results at valley-2 indicate that, during the  
 837 daytime, the aerosol-meteorology feedback increases the easterly wind speed but  
 838 decreases the southerly wind speed, resulting in decreased transport flux of BC towards  
 839 the TP; during the night, the aerosol-meteorology feedback increases the easterly wind

speed but decreases the northerly wind speed, leading to reduced BC transport flux away from the TP. It is to be emphasized that, at two typical mountain valley channels, the impact of aerosol-meteorology feedback on the BC transport flux averaged within 2000 m above the ground level (Table S3) are consistent with those averaged within 500 m above the ground level.

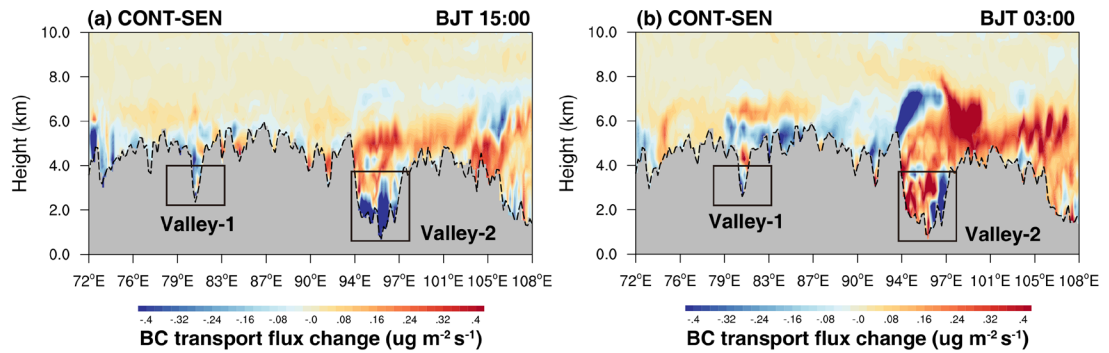


Figure 12. Difference in longitude–height cross section of BC transport flux along the cross line (shown as the blue dashed line in Figure 2) from the simulations with and without aerosol-meteorology feedback at 15:00 and 03:00 BJT averaged for the period from April 27 to May 4, 2016. The difference in PBLH along the cross section is shown here as the black dashed line.

Table 2. The mean zonal and meridional wind speeds at two typical valley channels within 500 m above the ground level at 15:00 and 03:00 BJT averaged for the period from April 27 to May 4, 2016 between the CONT and SEN experiments. The differences in zonal and meridional wind speeds between the two experiments are also shown. Positive value denotes a westerly or a southerly and negative value denotes an easterly or a northerly.

500 m	15:00	03:00
-------	-------	-------

		Valley-1	Valley-2	Valley-1	Valley-2
CONT	U component	2.32	-1.90	-1.34	-1.19
	V component	4.74	1.35	-1.73	-1.56
SEN	U component	2.75	-1.43	-1.26	-1.07
	V component	4.94	1.61	-1.60	-1.92
CONT-SEN	U component	-0.43	-0.47	-0.08	-0.12
	V component	-0.2	-0.26	-0.13	0.36

Similarly, to analyze the impact of aerosol-meteorology feedback on the vertically integrated trans-boundary transport flux of BC, the difference in longitudinal distribution of integrated BC transport flux along the cross line shown as the blue dashed line in Figure 2 from the simulations with and without aerosol-meteorology feedback is shown in Figure 13. As can be seen, with the aerosol-meteorology feedback, the integrated BC transport flux from central and western Himalayas (to the west of 88 °E) to the TP overall decreases; however, in the eastern Himalayas, the aerosol-meteorology feedback reduces the integrated transport flux of BC away from the TP (Figure 13). Therefore, the aerosol-meteorology feedback exerts substantial effect on cross-Himalayan transport flux of BC.

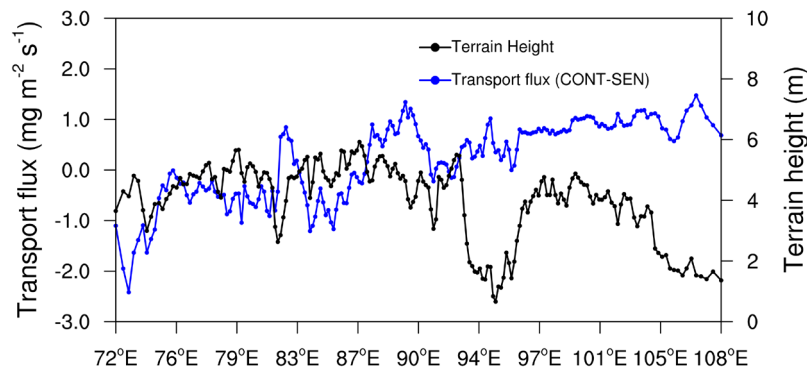


Figure 13. Difference in longitudinal distribution of vertically integrated BC transport flux along the cross section in Figure 2 from simulations with and without aerosol-meteorology feedback. The black line represents the terrain height.

## 4 Conclusion

The worst aerosol pollution episode ever recorded over the TP occurred during the period from April 20 to May 10, 2016. The observed largest AOD at reference sites of Nam Co and QOMS are 0.65 and 0.42, respectively. In this paper, the meteorological causes of this severe aerosol pollution event, the BC transport flux, and the aerosol-meteorology feedback as well as its effect on BC transport flux during this severe aerosol pollution event are investigated by using observational and reanalysis datasets and WRF-Chem simulation. By analyzing the evolution of weather maps at 500 hPa over the study area during this severe aerosol pollution event, it is found that the plateau vortex plays a critical role in increasing aerosol concentration in the inland of the TP. However, in the southern TP, the increase in aerosol concentration could be attributed to the long-range transport by southwesterly airflow in front of the trough.

With the acceptable performance of WRF-Chem model on simulating meteorological conditions and aerosols, we estimated the cross-Himalayan transport flux of BC. The results show that, in the central and western Himalayas, BC is imported into the TP during the day and night; however, in the eastern Himalayas, BC is imported into the TP during the day but exported slightly from the TP during the night; to the east of  $\sim 98^\circ\text{E}$ , BC is transported away from the TP during the day and night. The vertically integrated transport flux of BC along the cross line during the aerosol pollution event exhibits an overall decreasing trend from west to east, with the largest vertically integrated BC transport flux of  $20.8 \text{ mg m}^{-2} \text{ s}^{-1}$  occurring at the deepest mountain valley

in southwestern TP.

By designing experiments with or without aerosol-meteorology feedback, the feedback between aerosol and meteorology over the southern TP and IGP during this severe aerosol pollution event are investigated. It has been found that during the most polluted period from April 27 to May 4, aerosols lead to a slight change in surface air temperature in the southern TP but a significant decrease in surface air temperature with values in a range of 0.5–1.7 °C in the IGP. Vertically, in the southern TP, the largest temperature increase induced by aerosols occurs in the middle troposphere; however, in the IGP, aerosol-induced temperature decreases near the surface but increases in the middle troposphere. Spatially, the ARF is negative at the bottom of the atmosphere but is positive in the atmosphere. As a result, the atmospheric stratification over the study area is more stable. Additionally, affected by aerosols, U10 increases in the southern TP, with the largest increase of 0.2 m/s appearing at 19:00 BJT; while in the IGP, U10 decreases, with the largest decrease of 0.7 m/s appearing at 20:00 BJT. In respect to PBLH, aerosols lead to a decrease by 55 m in PBLH during 09:00–14:00 BJT and by 60 m during 17:00–20:00 BJT in the southern TP; whereas in the IGP, a decrease in PBLH resulted from aerosols mainly occurs during 10:00–20:00 BJT in the daytime, with the largest decrease of 1300 m detected at 20:00 BJT. Therefore, aerosols exert an important effect on meteorological conditions. By contrast, the aerosol-induced changes in meteorological conditions can lead to a decrease of surface BC concentration with value up to 0.16  $\mu\text{g}/\text{m}^3$  (50%) in the southern TP and an increase of surface BC concentration with value up to 2.2  $\mu\text{g}/\text{m}^3$  (75%) in the IGP.

By investigating the impact of aerosol-meteorology feedback on the BC transport flux, it has been acquired that, with the aerosol-meteorology feedback, the vertically integrated transport flux of BC from central and western Himalayas to the TP overall decreases; however, in the eastern Himalayas, the aerosol-meteorology feedback reduces the vertically integrated transport flux of BC away from the TP. In particular, the corresponding results at two typical mountain valley channels in southwestern and southeastern TP reveal that the aerosol-meteorology feedback decreases the import of BC towards the TP at mountain valley channel in southwestern TP during the daytime and nighttime, while at mountain valley channel in the southeastern TP, the feedback decreases the import of BC towards the TP during the daytime and reduces the BC transport flux away from the TP during the nighttime.

There are still uncertainties in this study. Because the aerosol direct effect is very sensitive to the mixing state between scattering aerosols and absorbing aerosols and the aerosol feedback derived from the aerosol radiative effect has large impacts during the daytime. By analyzing the model performance on aerosols, we find that the WRF-Chem model exhibited an underestimation for AOD in this study. This underestimation may have important effect on aerosol feedback during the most polluted period. Similarly, the BC transport flux quantified by WRF-Chem model also has bias to some extent. However, with very limited observational data over the TP, numerical model is the best tool for this study. Therefore, we plan to focus further research on a more accurate representation of the aerosol mixing state in models, in order to have a less uncertain simulation of the related optical properties. Also, to improve the model performance,

emissions with higher resolution and model with finer horizontal resolution will be used. In addition, we note that our results are based on a severe aerosol pollution event over a short period, and studies with longer duration are desirable in the future to test whether the results obtained from this severe aerosol pollution event are universal.

## **Data Availability Statement**

ERA-Interim reanalysis dataset is provided by European Centre for Medium-Range Weather Forecasts (<https://www.ecmwf.int/en/forecasts/datasets/reanalysis-datasets/era-interim>). The original simulation data used in this study are stored in a high-performance computing centre of Sun Yat-Sen University due to large data storage and can be made available from the corresponding author upon request. The ground-based AOD data are available through the AERONET website of <https://aeronet.gsfc.nasa.gov/>. The satellite-based AOD are available through the website of [https://ladsweb.modaps.eosdis.nasa.gov/archive/allData/61/MYD08\\_D3/](https://ladsweb.modaps.eosdis.nasa.gov/archive/allData/61/MYD08_D3/). The National Centers for Environmental Prediction (NCEP) Final Analysis (FNL) data are available through the website of <https://rda.ucar.edu/datasets/ds083.2/dataaccess/>. The Emission Database for Global Atmospheric Research (EDGAR)-Hemispheric Transport Air Pollution version 2 (HTAPv2) emission inventory is available through the website of [https://edgar.jrc.ec.europa.eu/dataset\\_htap\\_v2](https://edgar.jrc.ec.europa.eu/dataset_htap_v2). The Fire INventory from NCAR (FINN) is available through the website of <https://www.acom.ucar.edu/Data/fire/>. CAM-Chem data are available through University Corporation for Atmospheric Research (<https://www.acom.ucar.edu/cam-chem/cam-chem.shtml>).



## Author contributions

**Shichang Kang and Haipeng Yu:** Conceptualization, writing - review & editing.

**Yuling Hu:** Visualization, validation, writing - original draft. **Shichang Kang:**

Supervision. **Yuling Hu, Junhua Yang and Xintong Chen:** Methodology, software.

**Xiufeng Yin and Pengfei Chen:** Data curation, validation.

## Competing interests

The authors declare that they have no conflict of interest.

## Acknowledgments

This study was supported by the National Natural Science Foundation of China (42205123), the Gansu Province Science Foundation for Youths (23JRRA617), the Chinese Academy of Sciences (XDA20040501). The authors would like to acknowledge the National Centers for Environmental Prediction (NCEP) and the European Centre for Medium-Range Weather Forecasts (ECMWF) for providing final analysis data and reanalysis data, respectively. Finally, this work was supported by the National Key Scientific and Technological Infrastructure project “Earth System Numerical Simulation Facility” (EarthLab) and Supercomputing Center of Sun Yat-sen University.

## References

- Bran, S. H., and Srivastava, R.: Investigation of PM<sub>2.5</sub> mass concentration over India using a regional climate model, *Environ. Pollut.*, 224, 484-493, <https://doi.org/10.1016/j.envpol.2017.02.030>, 2017.
- Buchard, V., Randles, C. A., da Silva, A. M., Darmenov, A., Colarco, P. R., Govindaraju, R., Ferrare, R., Hair, J., Beyersdorf, A. J., Ziemba, L. D., and Yu, H.: The MERRA-2 Aerosol Reanalysis, 1980 Onward. Part II: Evaluation and Case Studies, *J. Clim.*, 30 (17), 6851-6872, <https://doi.org/10.1175/JCLI-D-16-0613.1>, 2017.
- Che, H., Gui, K., Xia, X., Wang, Y., Holben, B. N., Goloub, P., Cuevas-Agulló, E., Wang, H., Zheng, Y., Zhao, H., and Zhang, X.: Large contribution of meteorological factors to inter-decadal changes in regional

987 aerosol optical depth, *Atmos. Chem. Phys.*, 19 (16), 10497-10523, [https://doi.org/10.5194/acp-19-](https://doi.org/10.5194/acp-19-10497-2019)  
988 [10497-2019](https://doi.org/10.5194/acp-19-10497-2019), 2019.

989 Chen, L., Zhu, J., Liao, H., Gao, Y., Qiu, Y. L., Zhang, M. G., Liu, Z. R., Li, N., and Wang, Y. S.: Assessing the  
990 formation and evolution mechanisms of severe haze pollution in the Beijing-Tianjin-Hebei region using  
991 process analysis, *Atmos. Chem. Phys.*, 19 (16), 10845-10864, [https://doi.org/10.5194/acp-19-10845-](https://doi.org/10.5194/acp-19-10845-2019)  
992 [2019](https://doi.org/10.5194/acp-19-10845-2019), 2019a.

993 Chen, X., Kang, S., Cong, Z., Yang, J., and Ma, Y.: Concentration, temporal variation, and sources of black  
994 carbon in the Mt. Everest region retrieved by real-time observation and simulation, *Atmos. Chem. Phys.*,  
995 18 (17), 12859-12875, <https://doi.org/10.5194/acp-18-12859-2018>, 2018.

996 Chen, Y., Yang, K., Zhou, D., Qin, J., and Guo, X.: Improving the Noah Land Surface Model in Arid Regions  
997 with an Appropriate Parameterization of the Thermal Roughness Length, *J. Hydrometeorol.*, 11 (4), 995-  
998 1006, <https://doi.org/10.1175/2010JHM1185.1>, 2010.

999 Chen, Y., Zhou, Y., and Zhao, X.: PM<sub>2.5</sub> over North China based on MODIS AOD and effect of  
1000 meteorological elements during 2003–2015, *Front. Environ. Sci. Eng.*, 14 (2), 23,  
1001 <https://doi.org/10.1007/s11783-019-1202-8>, 2019b.

1002 Chin, M., Ginoux, P., Kinne, S., Torres, O., Holben, B. N., Duncan, B. N., Martin, R. V., Logan, J. A., Higurashi,  
1003 A., and Nakajima, T.: Tropospheric Aerosol Optical Thickness from the GOCART Model and Comparisons  
1004 with Satellite and Sun Photometer Measurements, *J. Atmos. Sci.*, 59 (3), 461-483,  
1005 [https://doi.org/10.1175/1520-0469\(2002\)059<0461:TAOTFT>2.0.CO;2](https://doi.org/10.1175/1520-0469(2002)059<0461:TAOTFT>2.0.CO;2), 2002.

1006 China, S., Scarnato, B., Owen, R. C., Zhang, B., Ampadu, M. T., Kumar, S., Dzepina, K., Dziobak, M. P.,  
1007 Fialho, P., Perlinger, J. A., Hueber, J., Helmig, D., Mazzoleni, L. R., and Mazzoleni, C.: Morphology and  
1008 mixing state of aged soot particles at a remote marine free troposphere site: Implications for optical  
1009 properties, *Geophys. Res. Lett.*, 42 (4), 1243-1250, <https://doi.org/10.1002/2014GL062404>, 2015.

1010 Chung, C. E., Ramanathan, V., Kim, D., and Podgorny, I. A.: Global anthropogenic aerosol direct forcing  
1011 derived from satellite and ground-based observations, *J. Geophys. Res.: Atmos.*, 110 (D24),  
1012 <https://doi.org/10.1029/2005JD006356>, 2005.

1013 Chung, C. E., Cha, H., Vihma, T., Räisänen, P., and Decremier, D.: On the possibilities to use atmospheric  
1014 reanalyses to evaluate the warming structure in the Arctic, *Atmos. Chem. Phys.*, 13 (22), 11209-11219,  
1015 <https://doi.org/10.5194/acp-13-11209-2013>, 2013.

1016 Colarco, P., da Silva, A., Chin, M., and Diehl, T.: Online simulations of global aerosol distributions in the  
1017 NASA GEOS-4 model and comparisons to satellite and ground-based aerosol optical depth, *J. Geophys.*  
1018 *Res.: Atmos.*, 115 (D14), <https://doi.org/10.1029/2009JD012820>, 2010.

1019 Duan, A., Wu, G., Zhang, Q., and Liu, Y.: New proofs of the recent climate warming over the Tibetan  
1020 Plateau as a result of the increasing greenhouse gases emissions, *Chin. Sci. Bull.*, 51 (11), 1396-1400,  
1021 <https://doi.org/10.1007/s11434-006-1396-6>, 2006.

1022 Dubovik, O., and King, M. D.: A flexible inversion algorithm for retrieval of aerosol optical properties  
1023 from Sun and sky radiance measurements, *J. Geophys. Res.: Atmos.*, 105 (D16), 20673-20696,  
1024 <https://doi.org/10.1029/2000JD900282>, 2000.

1025 Ek, M. B., Mitchell, K. E., Lin, Y., Rogers, E., Grunmann, P., Koren, V., Gayno, G., and Tarpley, J. D.:  
1026 Implementation of Noah land surface model advances in the National Centers for Environmental  
1027 Prediction operational mesoscale Eta model, *J. Geophys. Res.: Atmos.*, 108 (D22), 8851,  
1028 <https://doi.org/10.1029/2002JD003296>, 2003.

1029 Fast, J. D., Gustafson Jr, W. I., Easter, R. C., Zaveri, R. A., Barnard, J. C., Chapman, E. G., Grell, G. A., and  
1030 Peckham, S. E.: Evolution of ozone, particulates, and aerosol direct radiative forcing in the vicinity of

1031 Houston using a fully coupled meteorology-chemistry-aerosol model, *J. Geophys. Res.: Atmos.*, 111  
 1032 (D21), <https://doi.org/10.1029/2005JD006721>, 2006.  
 1033 Flanner, M. G., Zender, C. S., Randerson, J. T., and Rasch, P. J.: Present-day climate forcing and response  
 1034 from black carbon in snow, *J. Geophys. Res.: Atmos.*, 112 (D11), <https://doi.org/10.1029/2006JD008003>,  
 1035 2007.  
 1036 Gao, M., Carmichael, G. R., Wang, Y., Saide, P. E., Yu, M., Xin, J., Liu, Z., and Wang, Z.: Modeling study of  
 1037 the 2010 regional haze event in the North China Plain, *Atmos. Chem. Phys.*, 16 (3), 1673-1691,  
 1038 <https://doi.org/10.5194/acp-16-1673-2016>, 2016.  
 1039 Gao, Y., Zhang, M., Liu, Z., Wang, L., Wang, P., Xia, X., Tao, M., and Zhu, L.: Modeling the feedback  
 1040 between aerosol and meteorological variables in the atmospheric boundary layer during a severe fog–  
 1041 haze event over the North China Plain, *Atmos. Chem. Phys.*, 15 (8), 4279-4295,  
 1042 <https://doi.org/10.5194/acp-15-4279-2015>, 2015.  
 1043 Gelaro, R., McCarty, W., Suárez, M. J., Todling, R., Molod, A., Takacs, L., Randles, C. A., Darmenov, A.,  
 1044 Bosilovich, M. G., Reichle, R., Wargan, K., Coy, L., Cullather, R., Draper, C., Akella, S., Buchard, V., Conaty,  
 1045 A., da Silva, A. M., Gu, W., Kim, G.-K., Koster, R., Lucchesi, R., Merkova, D., Nielsen, J. E., Partyka, G.,  
 1046 Pawson, S., Putman, W., Rienecker, M., Schubert, S. D., Sienkiewicz, M., and Zhao, B.: The Modern-Era  
 1047 Retrospective Analysis for Research and Applications, Version 2 (MERRA-2), *J. Clim.*, 30 (14), 5419-5454,  
 1048 <https://doi.org/10.1175/JCLI-D-16-0758.1>, 2017.  
 1049 Grell, G. A., Peckham, S. E., Schmitz, R., McKeen, S. A., Frost, G., Skamarock, W. C., and Eder, B.: Fully  
 1050 coupled “online” chemistry within the WRF model, *Atmos. Environ.*, 39 (37), 6957-6975,  
 1051 <https://doi.org/10.1016/j.atmosenv.2005.04.027>, 2005.  
 1052 Grell, G. A., and Freitas, S. R.: A scale and aerosol aware stochastic convective parameterization for  
 1053 weather and air quality modeling, *Atmos. Chem. Phys.*, 14 (10), 5233-5250,  
 1054 <https://doi.org/10.5194/acp-14-5233-2014>, 2014.  
 1055 Guenther, A., Karl, T., Harley, P., Wiedinmyer, C., Palmer, P. I., and Geron, C.: Estimates of global  
 1056 terrestrial isoprene emissions using MEGAN (Model of Emissions of Gases and Aerosols from Nature),  
 1057 *Atmos. Chem. Phys.*, 6 (11), 3181-3210, <https://doi.org/10.5194/acp-6-3181-2006>, 2006.  
 1058 Guenther, A. B., Jiang, X., Heald, C. L., Sakulyanontvittaya, T., Duhl, T., Emmons, L. K., and Wang, X.: The  
 1059 Model of Emissions of Gases and Aerosols from Nature version 2.1 (MEGAN2.1): an extended and  
 1060 updated framework for modeling biogenic emissions, *Geosci. Model Dev.*, 5 (6), 1471-1492,  
 1061 <https://doi.org/10.5194/gmd-5-1471-2012>, 2012.  
 1062 Hansen, J., and Nazarenko, L.: Soot climate forcing via snow and ice albedos, *PNAS*, 101 (2), 423,  
 1063 <https://doi.org/10.1073/pnas.2237157100>, 2004.  
 1064 He, C., Liou, K. N., Takano, Y., Zhang, R., Levy Zamora, M., Yang, P., Li, Q., and Leung, L. R.: Variation of  
 1065 the radiative properties during black carbon aging: theoretical and experimental intercomparison,  
 1066 *Atmos. Chem. Phys.*, 15 (20), 11967-11980, <https://doi.org/10.5194/acp-15-11967-2015>, 2015.  
 1067 Heidinger, A. K., Foster, M. J., Walther, A., and Zhao, X.: The Pathfinder Atmospheres–Extended AVHRR  
 1068 Climate Dataset, *Bull. Am. Meteorol. Soc.*, 95 (6), 909-922, [https://doi.org/10.1175/BAMS-D-12-](https://doi.org/10.1175/BAMS-D-12-00246.1)  
 1069 [00246.1](https://doi.org/10.1175/BAMS-D-12-00246.1), 2014.  
 1070 Holben, B. N., Eck, T. F., Slutsker, I., Tanré, D., Buis, J. P., Setzer, A., Vermote, E., Reagan, J. A., Kaufman,  
 1071 Y. J., Nakajima, T., Lavenu, F., Jankowiak, I., and Smirnov, A.: AERONET—A Federated Instrument Network  
 1072 and Data Archive for Aerosol Characterization, *Remote Sens. Environ.*, 66 (1), 1-16,  
 1073 [https://doi.org/10.1016/S0034-4257\(98\)00031-5](https://doi.org/10.1016/S0034-4257(98)00031-5), 1998.  
 1074 Hong, C. P., Zhang, Q., Zhang, Y., Davis, S. J., Zhang, X., Tong, D., Guan, D. B., Liu, Z., and He, K. B.:

Weakening aerosol direct radiative effects mitigate climate penalty on Chinese air quality, *Nat. Clim. Change*, 10 (9), 845-850, <https://doi.org/10.1038/s41558-020-0840-y>, 2020.

Hsu, N. C., Jeong, M. J., Bettenhausen, C., Sayer, A. M., Hansell, R., Seftor, C. S., Huang, J., and Tsay, S. C.: Enhanced Deep Blue aerosol retrieval algorithm: The second generation, *J. Geophys. Res.: Atmos.*, 118 (16), 9296-9315, <https://doi.org/10.1002/jgrd.50712>, 2013.

Hu, Y., Kang, S., Yang, J., Chen, X., Ji, Z., and Rai, M.: Transport of black carbon from Central and West Asia to the Tibetan Plateau: Seasonality and climate effect, *Atmos. Res.*, 267, 105987, <https://doi.org/10.1016/j.atmosres.2021.105987>, 2022.

Iacono, M. J., Delamere, J. S., Mlawer, E. J., Shephard, M. W., Clough, S. A., and Collins, W. D.: Radiative forcing by long-lived greenhouse gases: Calculations with the AER radiative transfer models, *J. Geophys. Res.: Atmos.*, 113 (D13), <https://doi.org/10.1029/2008JD009944>, 2008.

Janjić, Z. I.: The Step-Mountain Eta Coordinate Model: Further Developments of the Convection, Viscous Sublayer, and Turbulence Closure Schemes, *Mon. Weather Rev.*, 122 (5), 927-945, [https://doi.org/10.1175/1520-0493\(1994\)122<0927:TSMECM>2.0.CO;2](https://doi.org/10.1175/1520-0493(1994)122<0927:TSMECM>2.0.CO;2), 1994.

Janssens-Maenhout, G., Crippa, M., Guizzardi, D., Dentener, F., Muntean, M., Pouliot, G., Keating, T., Zhang, Q., Kurokawa, J., Wankmüller, R., Denier van der Gon, H., Kuenen, J. J. P., Klimont, Z., Frost, G., Darras, S., Koffi, B., and Li, M.: HTAP\_v2.2: a mosaic of regional and global emission grid maps for 2008 and 2010 to study hemispheric transport of air pollution, *Atmos. Chem. Phys.*, 15 (19), 11411-11432, <https://doi.org/10.5194/acp-15-11411-2015>, 2015.

Ji, Z., Kang, S., Zhang, D., Zhu, C., Wu, J., and Xu, Y.: Simulation of the anthropogenic aerosols over South Asia and their effects on Indian summer monsoon, *Clim. Dyn.*, 36 (9-10), 1633-1647, <https://doi.org/10.1007/s00382-010-0982-0>, 2011.

Kahn, R. A., Gaitley, B. J., Martonchik, J. V., Diner, D. J., Crean, K. A., and Holben, B.: Multiangle Imaging Spectroradiometer (MISR) global aerosol optical depth validation based on 2 years of coincident Aerosol Robotic Network (AERONET) observations, *J. Geophys. Res.: Atmos.*, 110 (D10), <https://doi.org/10.1029/2004JD004706>, 2005.

Kang, S., Xu, Y., You, Q., Flügel, W.-A., Pepin, N., and Yao, T.: Review of climate and cryospheric change in the Tibetan Plateau, *Environ. Res. Lett.*, 5 (1), 015101, <https://doi.org/10.1088/1748-9326/5/1/015101>, 2010.

Kang, S., Cong, Z., Wang, X., Zhang, Q., Ji, Z., Zhang, Y., and Xu, B.: The transboundary transport of air pollutants and their environmental impacts on Tibetan Plateau, *Chin. Sci. Bull.*, 64 (27), 2876-2884, 2019a.

Kang, S., Zhang, Q., Qian, Y., Ji, Z., Li, C., Cong, Z., Zhang, Y., Guo, J., Du, W., Huang, J., You, Q., Panday, A. K., Rupakheti, M., Chen, D., Gustafsson, Ö., Thiemens, M. H., and Qin, D.: Linking atmospheric pollution to cryospheric change in the Third Pole region: current progress and future prospects, *Natl. Sci. Rev.*, 6 (4), 796-809, <https://doi.org/10.1093/nsr/nwz031>, 2019b.

Lau, K. M., Kim, M. K., and Kim, K. M.: Asian summer monsoon anomalies induced by aerosol direct forcing: the role of the Tibetan Plateau, *Clim. Dyn.*, 26 (7), 855-864, <https://doi.org/10.1007/s00382-006-0114-z>, 2006.

Lelieveld, J., Crutzen, P. J., Ramanathan, V., Andreae, M. O., Brenninkmeijer, C. A. M., Campos, T., Cass, G. R., Dickerson, R. R., Fischer, H., de Gouw, J. A., Hansel, A., Jefferson, A., Kley, D., de Laat, A. T. J., Lal, S., Lawrence, M. G., Lobert, J. M., Mayol-Bracero, O., Mitra, A. P., Novakov, T., Oltmans, S. J., Prather, K. A., Reiner, T., Rodhe, H., Scheeren, H. A., Sikka, D., and Williams, J.: The Indian Ocean Experiment: Widespread Air Pollution from South and Southeast Asia, in: Paul J. Crutzen: A Pioneer on Atmospheric

Chemistry and Climate Change in the Anthropocene, edited by: Crutzen, P. J., and Brauch, H. G., Springer International Publishing, Cham, 197-209, 2016.

Levy, R. C., Remer, L. A., Kleidman, R. G., Mattoo, S., Ichoku, C., Kahn, R., and Eck, T. F.: Global evaluation of the Collection 5 MODIS dark-target aerosol products over land, *Atmos. Chem. Phys.*, **10** (21), 10399-10420, <https://doi.org/10.5194/acp-10-10399-2010>, 2010.

Li, C., and Yanai, M.: The Onset and Interannual Variability of the Asian Summer Monsoon in Relation to Land–Sea Thermal Contrast, *J. Clim.*, **9** (2), 358-375, [https://doi.org/10.1175/1520-0442\(1996\)009<0358:TOAIVO>2.0.CO;2](https://doi.org/10.1175/1520-0442(1996)009<0358:TOAIVO>2.0.CO;2), 1996.

Li, C., Bosch, C., Kang, S., Andersson, A., Chen, P., Zhang, Q., Cong, Z., Chen, B., Qin, D., and Gustafsson, Ö.: Sources of black carbon to the Himalayan–Tibetan Plateau glaciers, *Nat. Commun.*, **7** (1), 12574, <https://doi.org/10.1038/ncomms12574>, 2016a.

Li, J. W., Han, Z. W., Wu, Y. F., Xiong, Z., Xia, X. G., Li, J., Liang, L., and Zhang, R. J.: Aerosol radiative effects and feedbacks on boundary layer meteorology and PM(2.5 )chemical components during winter haze events over the Beijing-Tianjin-Hebei region, *Atmos. Chem. Phys.*, **20** (14), 8659-8690, <https://doi.org/10.5194/acp-20-8659-2020>, 2020.

Li, Z., Lau, W. K. M., Ramanathan, V., Wu, G., Ding, Y., Manoj, M. G., Liu, J., Qian, Y., Li, J., Zhou, T., Fan, J., Rosenfeld, D., Ming, Y., Wang, Y., Huang, J., Wang, B., Xu, X., Lee, S. S., Cribb, M., Zhang, F., Yang, X., Zhao, C., Takemura, T., Wang, K., Xia, X., Yin, Y., Zhang, H., Guo, J., Zhai, P. M., Sugimoto, N., Babu, S. S., and Brasseur, G. P.: Aerosol and monsoon climate interactions over Asia, *Rev. Geophys.*, **54** (4), 866-929, <https://doi.org/10.1002/2015RG000500>, 2016b.

Liu, T., Gong, S., He, J., Yu, M., Wang, Q., Li, H., Liu, W., Zhang, J., Li, L., Wang, X., Li, S., Lu, Y., Du, H., Wang, Y., Zhou, C., Liu, H., and Zhao, Q.: Attributions of meteorological and emission factors to the 2015 winter severe haze pollution episodes in China's Jing-Jin-Ji area, *Atmos. Chem. Phys.*, **17** (4), 2971-2980, <https://doi.org/10.5194/acp-17-2971-2017>, 2017.

Liu, Y., Jia, R., Dai, T., Xie, Y., and Shi, G.: A review of aerosol optical properties and radiative effects, *J. Meteorol. Res.*, **28** (6), 1003-1028, <https://doi.org/10.1007/s13351-014-4045-z>, 2014.

Meehl, G. A.: Coupled Land-Ocean-Atmosphere Processes and South Asian Monsoon Variability, *Science*, **266** (5183), 263-267, <https://doi.org/10.1126/science.266.5183.263>, 1994.

Menon, S., Hansen, J., Nazarenko, L., and Luo, Y.: Climate Effects of Black Carbon Aerosols in China and India, *Science*, **297** (5590), 2250-2253, <https://doi.org/10.1126/science.1075159>, 2002.

Morrison, H., Thompson, G., and Tatarskii, V.: Impact of Cloud Microphysics on the Development of Trailing Stratiform Precipitation in a Simulated Squall Line: Comparison of One- and Two-Moment Schemes, *Mon. Weather Rev.*, **137** (3), 991-1007, <https://doi.org/10.1175/2008MWR2556.1>, 2009.

O'Neill, N. T., Eck, T. F., Smirnov, A., Holben, B. N., and Thulasiraman, S.: Spectral discrimination of coarse and fine mode optical depth, *J. Geophys. Res.: Atmos.*, **108** (D17), <https://doi.org/10.1029/2002JD002975>, 2003.

O'Neill, N. T., Pancrati, O., Baibakov, K., Eloranta, E., Batchelor, R. L., Freemantle, J., McArthur, L. J. B., Strong, K., and Lindenmaier, R.: Occurrence of weak, sub-micron, tropospheric aerosol events at high Arctic latitudes, *Geophys. Res. Lett.*, **35** (14), <https://doi.org/10.1029/2008GL033733>, 2008.

Pokharel, M., Guang, J., Liu, B., Kang, S., Ma, Y., Holben, B., Xia, X. a., Xin, J., Ram, K., Rupakheti, D., Xin, W., Wu, G., Bhattarai, H., Zhao, C., and Cong, Z.: Aerosol Properties Over Tibetan Plateau From a Decade of AERONET Measurements: Baseline, Types, and Influencing Factors, *J. Geophys. Res.: Atmos.*, **124**, <https://doi.org/10.1029/2019JD031293>, 2019.

Qian, Y., Flanner, M. G., Leung, L. R., and Wang, W.: Sensitivity studies on the impacts of Tibetan Plateau

snowpack pollution on the Asian hydrological cycle and monsoon climate, *Atmos. Chem. Phys.*, 11 (5), 1929-1948, <https://doi.org/10.5194/acp-11-1929-2011>, 2011.

Qin, Y., and Xie, S. D.: Spatial and temporal variation of anthropogenic black carbon emissions in China for the period 1980–2009, *Atmos. Chem. Phys.*, 12 (11), 4825-4841, <https://doi.org/10.5194/acp-12-4825-2012>, 2012.

Qiu, Y. L., Liao, H., Zhang, R. J., and Hu, J. L.: Simulated impacts of direct radiative effects of scattering and absorbing aerosols on surface layer aerosol concentrations in China during a heavily polluted event in February 2014, *J. Geophys. Res.: Atmos.*, 122 (11), 5955-5975, <https://doi.org/10.1002/2016JD026309>, 2017.

Rai, M., Kang, S., Yang, J., Chen, X., Hu, Y., and Rupakheti, D.: Tracing Atmospheric Anthropogenic Black Carbon and Its Potential Radiative Response Over Pan-Third Pole Region: A Synoptic-Scale Analysis Using WRF-Chem, *J. Geophys. Res.: Atmos.*, 127 (6), e2021JD035772, <https://doi.org/10.1029/2021JD035772>, 2022.

Ramanathan, V., Chung, C., Kim, D., Bettge, T., Buja, L., Kiehl, J. T., Washington, W. M., Fu, Q., Sikka, D. R., and Wild, M.: Atmospheric brown clouds: Impacts on South Asian climate and hydrological cycle, *PNAS*, 102 (15), 5326, <https://doi.org/10.1073/pnas.0500656102>, 2005.

Ramanathan, V., and Carmichael, G.: Global and regional climate changes due to black carbon, *Nat. Geosci.*, 1 (4), 221-227, <https://doi.org/10.1038/ngeo156>, 2008.

Randles, C. A., da Silva, A. M., Buchard, V., Colarco, P. R., Darmenov, A., Govindaraju, R., Smirnov, A., Holben, B., Ferrare, R., Hair, J., Shinozuka, Y., and Flynn, C. J.: The MERRA-2 Aerosol Reanalysis, 1980 Onward. Part I: System Description and Data Assimilation Evaluation, *J. Clim.*, 30 (17), 6823-6850, <https://doi.org/10.1175/JCLI-D-16-0609.1>, 2017.

Shi, Y., Bilal, M., Ho, H. C., and Omar, A.: Urbanization and regional air pollution across South Asian developing countries – A nationwide land use regression for ambient PM<sub>2.5</sub> assessment in Pakistan, *Environ. Pollut.*, 266, 115145, <https://doi.org/10.1016/j.envpol.2020.115145>, 2020.

Skiles, S. M., Flanner, M., Cook, J. M., Dumont, M., and Painter, T. H.: Radiative forcing by light-absorbing particles in snow, *Nat. Clim. Change*, 8 (11), 964-971, <https://doi.org/10.1038/s41558-018-0296-5>, 2018.

Smirnov, A., Holben, B. N., Slutsker, I., Giles, D. M., McClain, C. R., Eck, T. F., Sakerin, S. M., Macke, A., Croot, P., Zibordi, G., Quinn, P. K., Sciare, J., Kinne, S., Harvey, M., Smyth, T. J., Piketh, S., Zielinski, T., Proshutinsky, A., Goes, J. I., Nelson, N. B., Larouche, P., Radionov, V. F., Goloub, P., Krishna Moorthy, K., Matarrese, R., Robertson, E. J., and Jourdin, F.: Maritime Aerosol Network as a component of Aerosol Robotic Network, *J. Geophys. Res.: Atmos.*, 114 (D6), <https://doi.org/10.1029/2008JD011257>, 2009.

Srivastava, P., and Sharan, M.: An Analytical Formulation of the Monin–Obukhov Stability Parameter in the Atmospheric Surface Layer Under Unstable Conditions, *Boundary Layer Meteorol.*, 165 (2), 371-384, <https://doi.org/10.1007/s10546-017-0273-y>, 2017.

Sun, E., Xu, X., Che, H., Tang, Z., Gui, K., An, L., Lu, C., and Shi, G.: Variation in MERRA-2 aerosol optical depth and absorption aerosol optical depth over China from 1980 to 2017, *J. Atmos. Sol. Terr. Phys.*, 186, 8-19, <https://doi.org/10.1016/j.jastp.2019.01.019>, 2019.

Wang, P., Guo, H., Hu, J., Kota, S. H., Ying, Q., and Zhang, H.: Responses of PM<sub>2.5</sub> and O<sub>3</sub> concentrations to changes of meteorology and emissions in China, *Sci. Total Environ.*, 662, 297-306, <https://doi.org/10.1016/j.scitotenv.2019.01.227>, 2019.

Wiedinmyer, C., Akagi, S. K., Yokelson, R. J., Emmons, L. K., Al-Saadi, J. A., Orlando, J. J., and Soja, A. J.: The Fire INventory from NCAR (FINN): a high resolution global model to estimate the emissions from open burning, *Geosci. Model Dev.*, 4 (3), 625-641, <https://doi.org/10.5194/gmd-4-625-2011>, 2011.



1207 Wu, G., Liu, Y., Zhang, Q., Duan, A., Wang, T., Wan, R., Liu, X., Li, W., Wang, Z., and Liang, X.: The Influence  
1208 of Mechanical and Thermal Forcing by the Tibetan Plateau on Asian Climate, *J. Hydrometeorol.*, **8** (4),  
1209 770-789, <https://doi.org/10.1175/JHM609.1>, 2007.

1210 Wu, J., Fu, C., Xu, Y., Tang, J. P., Wang, W., and Wang, Z.: Simulation of direct effects of black carbon  
1211 aerosol on temperature and hydrological cycle in Asia by a Regional Climate Model, *Meteorol. Atmos.*  
1212 *Phys.*, **100** (1), 179-193, <https://doi.org/10.1007/s00703-008-0302-y>, 2008.

1213 Wu, J. R., Bei, N. F., Hu, B., Liu, S. X., Zhou, M., Wang, Q. Y., Li, X., Liu, L., Feng, T., Liu, Z. R., Wang, Y. C.,  
1214 Cao, J. J., Tie, X. X., Wang, J., Molina, L. T., and Li, G. H.: Aerosol-radiation feedback deteriorates the  
1215 wintertime haze in the North China Plain, *Atmos. Chem. Phys.*, **19** (13), 8703-8719,  
1216 <https://doi.org/10.5194/acp-19-8703-2019>, 2019.

1217 Xu, B., Cao, J., Hansen, J., Yao, T., Joswila, D. R., Wang, N., Wu, G., Wang, M., Zhao, H., Yang, W., Liu, X.,  
1218 and He, J.: Black soot and the survival of Tibetan glaciers, *PNAS*, **106** (52), 22114,  
1219 <https://doi.org/10.1073/pnas.0910444106>, 2009.

1220 Yanai, M., Li, C., and Song, Z.: Seasonal Heating of the Tibetan Plateau and Its Effects on the Evolution  
1221 of the Asian Summer Monsoon, *Journal of the Meteorological Society of Japan. Ser. II*, **70** (1B), 319-351,  
1222 [https://doi.org/10.2151/jmsj1965.70.1B\\_319](https://doi.org/10.2151/jmsj1965.70.1B_319), 1992.

1223 Yang, J., Kang, S., Ji, Z., and Chen, D.: Modeling the origin of anthropogenic black carbon and its climatic  
1224 effect over the Tibetan Plateau and surrounding regions, *J. Geophys. Res.: Atmos.*, **123** (2), 671-692,  
1225 <https://doi.org/10.1002/2017JD027282>, 2018.

1226 Yao, T., Pu, J., Lu, A., Wang, Y., and Yu, W.: Recent Glacial Retreat and Its Impact on Hydrological  
1227 Processes on the Tibetan Plateau, China, and Surrounding Regions, *Arctic, Antarctic, and Alpine*  
1228 *Research*, **39** (4), 642-650, [https://doi.org/10.1657/1523-0430\(07-510\)\[YAO\]2.0.CO;2](https://doi.org/10.1657/1523-0430(07-510)[YAO]2.0.CO;2), 2007.

1229 Yao, T., Bolch, T., Chen, D., Gao, J., Immerzeel, W., Piao, S., Su, F., Thompson, L., Wada, Y., Wang, L., Wang,  
1230 T., Wu, G., Xu, B., Yang, W., Zhang, G., and Zhao, P.: The imbalance of the Asian water tower, *Nat. Rev.*  
1231 *Earth Env.*, <https://doi.org/10.1038/s43017-022-00299-4>, 2022.

1232 You, Q., Min, J., and Kang, S.: Rapid warming in the Tibetan Plateau from observations and CMIP5  
1233 models in recent decades, *Int. J. Climatol.*, **36** (6), 2660-2670, <https://doi.org/10.1002/joc.4520>, 2016.

1234 You, Q., Cai, Z., Pepin, N., Chen, D., Ahrens, B., Jiang, Z., Wu, F., Kang, S., Zhang, R., Wu, T., Wang, P., Li,  
1235 M., Zuo, Z., Gao, Y., Zhai, P., and Zhang, Y.: Warming amplification over the Arctic Pole and Third Pole:  
1236 Trends, mechanisms and consequences, *Earth Sci. Rev.*, **217**, 103625,  
1237 <https://doi.org/10.1016/j.earscirev.2021.103625>, 2021.

1238 Zaveri, R. A., and Peters, L. K.: A new lumped structure photochemical mechanism for large-scale  
1239 applications, *J. Geophys. Res.: Atmos.*, **104** (D23), 30387-30415, <https://doi.org/10.1029/1999JD900876>,  
1240 1999.

1241 Zaveri, R. A., Easter, R. C., Fast, J. D., and Peters, L. K.: Model for Simulating Aerosol Interactions and  
1242 Chemistry (MOSAIC), *J. Geophys. Res.: Atmos.*, **113** (D13204),  
1243 <https://doi.org/https://doi.org/10.1029/2007JD008782>, 2008.

1244 Zhang, M., Zhao, C., Cong, Z., Du, Q., Xu, M., Chen, Y., Chen, M., Li, R., Fu, Y., Zhong, L., Kang, S., Zhao,  
1245 D., and Yang, Y.: Impact of topography on black carbon transport to the southern Tibetan Plateau during  
1246 the pre-monsoon season and its climatic implication, *Atmos. Chem. Phys.*, **20** (10), 5923-5943,  
1247 <https://doi.org/10.5194/acp-20-5923-2020>, 2020.

1248 Zhang, X., Xu, X., Ding, Y., Liu, Y., Zhang, H., Wang, Y., and Zhong, J.: The impact of meteorological changes  
1249 from 2013 to 2017 on PM2.5 mass reduction in key regions in China, *Science China Earth Sciences*, **62**  
1250 (12), 1885-1902, <https://doi.org/10.1007/s11430-019-9343-3>, 2019.

Zhang, X. Y., Zhong, J. T., Wang, J. Z., Wang, Y. Q., and Liu, Y. J.: The interdecadal worsening of weather conditions affecting aerosol pollution in the Beijing area in relation to climate warming, *Atmos. Chem. Phys.*, **18** (8), 5991-5999, <https://doi.org/10.5194/acp-18-5991-2018>, 2018.

Zhang, Y., Gao, T., Kang, S., Shangguan, D., and Luo, X.: Albedo reduction as an important driver for glacier melting in Tibetan Plateau and its surrounding areas, *Earth Sci. Rev.*, **220**, 103735, <https://doi.org/10.1016/j.earscirev.2021.103735>, 2021.

Zhao, B., Liou, K. N., Gu, Y., Li, Q. B., Jiang, J. H., Su, H., He, C. L., Tseng, H. L. R., Wang, S. X., Liu, R., Qi, L., Lee, W. L., and Hao, J. M.: Enhanced PM<sub>2.5</sub> pollution in China due to aerosol-cloud interactions, *Sci. Rep.*, **7**, <https://doi.org/10.1038/s41598-017-04096-8>, 2017.

Zheng, B., Zhang, Q., Zhang, Y., He, K. B., Wang, K., Zheng, G. J., Duan, F. K., Ma, Y. L., and Kimoto, T.: Heterogeneous chemistry: a mechanism missing in current models to explain secondary inorganic aerosol formation during the January 2013 haze episode in North China, *Atmos. Chem. Phys.*, **15** (4), 2031-2049, <https://doi.org/10.5194/acp-15-2031-2015>, 2015.

Zhong, J. T., Zhang, X. Y., Dong, Y. S., Wang, Y. Q., Liu, C., Wang, J. Z., Zhang, Y. M., and Che, H. C.: Feedback effects of boundary-layer meteorological factors on cumulative explosive growth of PM<sub>2.5</sub> during winter heavy pollution episodes in Beijing from 2013 to 2016, *Atmos. Chem. Phys.*, **18** (1), 247-258, <https://doi.org/10.5194/acp-18-247-2018>, 2018.